LUND UNIVERSITY

Master of Science Thesis

A small-scale dosimetry model of the liver tissue

Anna Stenvall

Supervisors:

Bo-Anders Jönsson
Erik Larsson
Sven-Erik Strand

Department of Medical Radiation Physics
Clinical Sciences, Lund
Lund University, Sweden
2012

Abstract

Introduction: There is a need of reassessment of radiation absorbed dose specification in nuclear medicine, taking the non-uniformities in the distribution of radioactivity into account. This is especially important in radionuclide therapies where very high activities are administered and the radionuclides emit alpha particles, beta particles or low-energy electron and will require absorbed dose calculations on a scale comparable to the ranges of these particles. Although the liver is relatively radioresistant, this treatment rationale for radionuclide therapy has made the liver to be one of the dose-limiting organs. In this work we developed a small-scale dosimetry model of the liver, for Monte Carlo calculations of detailed and more accurate absorbed dose distributions of the liver microstructure.

Material and method: The mathematical model created, based on the microstructure of the hepatic lobule, is used to calculate absorbed doses on a tissue level for different radionuclides and for different source-target combinations within the liver. The Monte Carlo codes MCNP5, Version 1.51 and MCNPX 2.6 were used to create the model, consisting of a close packed hexagonal lattice pattern representing the hepatic lobules with the edge length of 500 μm, each centered around the central vein and in the periphery framed by six portal triads; *i.e.* the portal vein, the hepatic artery and the bile duct. The lobule section consists mainly of the hepatocytes, the bile canaliculi, the space of Disse and the mononuclear phagocytosis system, *i.e.* the Kupffer cells. Absorbed energy for different common radionuclides; ^{125}I, ^{90}Y, ^{211}At, ^{99}Tc^{m}, ^{111}In, ^{177}Lu, ^{131}I and ^{18}F were in different structures tallied and absorbed dose ratios between absorbed dosed in different targets and the mean absorbed dose to the total volume were calculated.

Results: Depending on the particles emitted and their energy the absorbed dose in different microstructures will differ. For nuclides emitting low energy particles, *e.g.* ^{125}I, the ratio between the locally absorbed dose and the mean dose the whole organ will be high; in the Kupffer cell acting as source about 135 times whereas in the hepatocytes close to the source the absorbed dose is close to the mean dose but significantly lower in areas between the Kupffer cells. For ^{90}Y on the other hand, the absorbed dose ratio in all target regions will be close to 1. For ^{111}In, used in diagnostics, the absorbed dose ratio will be quite comparable to ^{177}Lu, commonly used for the therapy. For the central vein, a possible target for radiation induced liver disease; the absorbed dose ratio will be as lowest for ^{177}Lu whereas the use of ^{90}Y and ^{18}F will result in an absorbed dose close to the mean dose.

Discussion: The small-scale dosimetry model created is a simplification of the organization of the hepatic microstructure and therefore the results will visualize an idealized situation and the numerical values presented may not represent the biological reality. Since the dose-response relation of the non-uniform absorbed dose distribution for different commonly used radionuclides is not known, the biological implications still need to be investigated.

Conclusion: A heterogeneous activity distribution will for some radionuclides result in a non-uniform absorbed dose distribution. Compared to the mean absorbed dose to the total volume of the liver, both over- and under-estimations of the absorbed dose can be seen, results which can have implications both in outcome of radionuclide therapies and for radiation risk estimations.

Populärvetenskaplig sammanfattning på svenska

Stor betydelse av dosimetrisk beräkning på liten skala. Vilken absorberad dos får den enskillda levercellen?

Att behandla tumörsjukdomar genom injektion av radioaktiva läkemedel är en behandlingsteknik kallad radionuklidterapi. Det radioaktiva läkemedlet består av en radioaktiv isotop, fäst på en målsökande bärarmolekyl, specifik för den vävnad vari man önskar att läkemedlet skall ansamlas. Då den radioaktiva isotopen sönderfaller sänds joniserande strålning ut; strålning med förmågan att jonisera molekyler i den vävnad den sänds ut. Jonisering av vävnad kan medföra skador på DNA i cellkärnan, vilket kan leda till att cellen slutar fungerar, eller till och med dör. För en tumörcell är detta ett önskvärt resultat; selektiv, lokal och målsökande strålbehandling.

Då strålningen från en radioaktiv isotop sänds ut i ett medium kommer den att på olika sätt växelverka med materian, varpå strålningen genom energiavgivning till mediet kommer att bromsas in och så småningom absorberas. Denna energiavgivning är den bakomliggande orsaken till joniseringen av mediet, varpå en ökad energideponering ökar antalet inträffade skador på DNA. Ett mått på denna energideponering anges som deponerad energi per massenhet och anges i enheten gray [Gy] och kallas absorberad dos.

Att beräkna den absorberade dosen är av intresse för att kunna optimera radionuklidterapin och således minska bieffekterna av stålningen på den friska vävnaden. Då den absorberade energin inuti en levande vävnad är en storhet som inte går att mäta, måste en beräkning genomföras för att erhålla en uppskattning av den absorberade dosen. Grunden för storheten absorberad dos är deponering av emitterad energi, en deponering som beror på de emitterade partiklarnas transport genom ett medium. Denna transport kan inte enkelt beräknas analytiskt, utan måste med hjälp av ett datorprogram, ett så kallat Monte Carlo program, simuleras fram.

Simulering av partiklars väg genom ett medium kräver en datormodell som beskriver dess geometri. De konventionella modellerna för att beräkna absorberad dos i mänskliga organ använder sig av en mycket förenklad bild av vävnaden, vilket leder till en osäker beräkning av den absorberade dosen. Syftet med detta projekt var att konstruera en mer noggrann modell av levervävnaden, för att på cellnivå kunna bestämma den absorberade dosen och således öka förståelsen för den absorberade dosens samband med den biologiska effekten.

Nya radionuklidbehandlingar har under de senaste åren introducerats i den kliniska verksamheten, behandlingar där mycket höga aktiviteter levereras för att uppnå absorberade doser höga nog för gott behandlingsresultat. Riskanalysen för frisk vävnad blir således än viktigare, varpå vikten av att kunna utföra rimligen adekvata absorberade dosberäkningar på en liten skala är stor.

I detta arbete har en realistisk modell av levervävnadens cellulära struktur skapats, baserad på morfologin av leverns funktionella enhet. Modellen kan således användas till att beräkna lokalt absorberade doser till de enskillda levercellerna, en absorberad dosberäkning mer detaljerad än den medelabsorberade dos vilken levereas med dagens beräkningsmodeller.

Table of contents

List of abbreviations

3D	Three dimensional
CT	Computer tomography
CV	Central vein
ESTEP	Electron substep
Eq	Equation
DSB	Double Strand Break
Dn	Distribution number
HCC	HepatoCellular Carcinoma
MC	Monte Carlo
MCNP	Monte Carlo N-Particles
MCNPX	Monte Carlo N-Particles eXtended
MIRD	Medical Internal Radiation Dose
MTD	Maximum Tolerable Dose
PDF	Probability density function
RES	Reticuloendothelial System
RILD	Radiation Induced Liver Disease
ROS	Reactive Oxygen Species
SEM	Scanning Electron Microscopy
SDEF	General Source Card
SIn	Source Information number
SIRT	Selective Internal Radiation Therapy
SPn	Source Probability number
TD	Tolerance Dose
u	Universe
VOD	Veno-Occlusive Disease

1 Introduction

1.1 Background

Radionuclide therapies of today will need a modified formulation of the absorbed dose specification, where the heterogeneous distribution in tissue of radiopharmaceuticals, intended or unintended, is taken into account. New treatment modalities where the activity distribution, and hence the absorbed dose distribution are known to be non-uniform, are treatments using radiolabeled microspheres implying a very localized treatment. Also for treatments using other radiopharmaceuticals, *e.g.* radiolabeled antibodies or colloids evidences have been shown indicating an undesired high accumulation within the liver tissue, seen on the macroscopic scale in combination with a heterogeneous distribution seen on the microstructural scale.

Of special importance of a modified absorbed dose specification are radionuclide therapies where very high activities will be delivered to the patient to obtain absorbed doses high enough for a successful treatment. Absorbed dose calculations to non-target areas, *i.e.* the normal cells in the organ, therefore are of great interest, especially since the liver for some treatment modalities have become one of the dose-limiting organs, even though the liver is a relatively radioresistant tissue.

The biological effect of internal emitters highly depends on the specific kind of radiation emitted and the distribution of the activity on a macroscopic, microscopic and cellular level, allowing concerns to be taken concerning a possible heterogeneous distribution of radiopharmaceuticals. Since the biological effects are expressed at the cellular level, also the dosimetric calculations should be, giving the absorbed dose to the microstructure of normal tissue and pathologic tissue, radiosensitive or not.

Most conventional dosimetric methodologies *e.g.* the Medical Internal Radiation Dose (MIRD) Committee of the Society of Nuclear Medicine method [1, 2], used today for the estimations of absorbed dose from internal emitters assume a uniform distribution of the radionuclides in an organ of homogenous composition large enough for edge effect to be negligible, an assumption known as the uniform isotropic model. Therefore the absorbed dose to the whole organ is presented as the averaged absorbed dose to the whole volume of the organ. Thus these conventional methods implicitly state that the absorbed dose to all individual cells of an organ is the same as the average absorbed dose to entire organ. This is applicable under the circumstances that the radionuclides accumulated in the source organ are emitting merely photons and high energy electrons, *i.e.* particles having a range in tissue longer than the length of the microstructures. However, for radionuclides whose decay results in the emission of alpha particles, beta particles or low energy electrons, the homogeneity assumption may be quite inadequate to describe the absorbed dose on a cellular level.

Since there are numerous studies showing observations of heterogeneity in the radionuclide uptake, both within organs [3-6] and within tumors [7], the estimation of the imparted energy to individual cells in the surrounding of cells with accumulated activity is of great interest.

In 1992 Jönsson *et al.* [3] presented a quantitative autoradiographic method to evaluate heterogeneous activity distribution in tissue after injection of different ^{111}In-labeled radiopharmaceuticals. Heterogeneous distribution, on an almost macroscopic scale were found in several tissues, among others the liver, which showed a grainy activity pattern. Already in 1988, Hindie *et al.* [4] had showed that the radionuclide distribution in the rat liver after injection of ^{99}Tc^{m}-sulphur colloids is heterogeneous and that the colloids

preferentially were located in the liver specific phagocytic macrophages, called Kupffer cells, well known for their phagocytizing properties [8, 9].

In 1990 Makrigiorgos *et al.* [5] undertook an experimental examination to determine the inhomogeneous deposition of radiopharmaceuticals in mouse liver and the subsequent dosimetric implications. They found that the injected $^{99}Tc^{m}$-labeled colloid intracellular-to-extracellular radioactivity concentration was 200- to 1000-fold in the hepatic macrophages, results expected to be applicable also to the human liver. Makrigiorgos *et al.* also performed dosimetric calculations; modeling the liver as a multicellular cluster of cells, represented by spheres arranged in a hexagonal pattern. Input was the fraction of the liver volume occupied by labeled Kupffer cells and the intra-to-extracellular radionuclide concentration and the output indicated that conventional dosimetry calculations underestimate the absorbed dose to the Kupffer cells of the human liver 8- to 30-fold.

In 1992 Gardin *et al.* [6] also performed a study trying to estimate the absorbed dose to these Kupffer cells after injection of $^{99}Tc^{m}$-sulphur colloids in rats. It was shown that only 0,2 % of the Kupffer cells were active in the phagocytosis of the radioactive colloids, but that 15 % of the totally emitted energy from electrons was absorbed within these macrophages. Gardin *et al.* approximated the Kupffer cells as spherical source regions, a simple model allowing the calculations of the absorbed dose in the Kupffer cell. The integral of the absorbed dose rate; given by the product of the activity of the source, the number of emitted particles, initial emitted energy of the particles and the fraction of the emitted energy absorbed at a specific distance gives an approximation of the absorbed dose within the cell itself. An extrapolation of these results to humans, Gardin et al approximates that the dose to the active Kupffer cells can be between 0,5 and 0,9 Gy/MBq, representing about 15000 times the average dose to the liver, according to macroscopic methods of mean absorbed dose estimations.

Makrigiorgos *et al.* [5] as well as Gardin *et al.* [6] performed calculations indicating a large, even though quite diverse, difference between the conventional dosimetry calculations for the average dose in the whole organ, compared to the dose calculation on a cellular level, where a heterogeneous activity pattern was taken into account.

Acting as a conclusion in the Makrigiorgos article [5] three conclusions concerning when the homogenous assumption of radionuclide distribution may lead to great miscalculations of the absorbed dose to individual cells were presented, concluding that dosimetric inaccuracies occurs when the radionuclide is: (A) taken up by a small fraction of the cells, (B) accumulated intracellular rather than extracellular and (C) emits short range radiation.

During the last years some small-scale dosimetry models (for additional reading, see chapter 2.2.2), which takes the heterogeneous activity distribution into account, and enabling concern to be taken to the A, B and C conclusions drawn by Makrigiorgos *et al.* [5], have been developed, [10-13]. Focus of the majority of these models has been to model hollow organs, such as the organs in the gastrointestinal tract, *e.g.* small and large intestines, to be able to determine the absorbed dose to the radiosensitive crypt cells. Also models simulating special treatment situations exist, i.e. on from Gulec *et al.* [14] simulating the dose distribution after administration of ^{90}Y microsphere in the hepatic artery. The overall conclusions of these articles are that absorbed dose calculations based on small-scale dosimetry models differs from the conventional dosimetric methodologies calculating an absorbed dose for a larger structure.

Conventional dosimetric methodologies, like the MIRD method [1, 2] are expressed to be sufficiently general for the dosimetry calculations of internal emitters, such that they can be applied to sources and targets of any dimension; from organs to microstructure,

cellular and subcellular components, giving us the possibility to calculate S-factors for different defined microstructures within the small-scale dosimetry model. The pros and cons of this concept was discussed by Howell [15] in 1994, highlighting the ability of the conventional dosimetry methods to subdivide the traditional organs into a number of subregions, making individual cells serve as 'organs'. Therefore, the uniform isotropic model will still be valid and S-values can be calculated for subcellular, cellular or multicellular geometries, thereby enabling absorbed dose calculations at these ranges.

New treatment techniques, many already in clinical use, will require new and more specific dosimetric models for absorbed dose calculations. Selective internal radiation therapy, SIRT, using ^{90}Y-microspheres for directed therapy to metastatic lesions in the liver, is a method to create point sources of radiation that preferentially accumulates in the peri- and intratumoral arterial vasculature [16]. The microspheres are neither metabolized nor excreted, wherefore the effective half-life is equal to the physical half-life and the microspheres will persist in the body even after the therapy [16]. The normal tissue adjacent to deposition locations of the radiolabeled microspheres will be exposed to the energy emitted from the radionuclides. A calculation of the absorbed dose to normal tissue for this relatively new treatment procedure therefore is of interest; both to be able to analyze the absorbed dose to individual cells adjacent to areas of uptake, but also for analyze of the absorbed dose gradient in the liver tissue from an area of high uptake.

Other therapies of interest are therapies using radiolabeled antibodies, where a very high uptake in the liver is observed in, for example Single Photon Emission Computed Tomography (SPECT) images of the abdomen of patients after injection of the radiopharmaceutical.

Since normal tissue dosimetry often is used to determine the maximum safe administered activity in radionuclide therapy, the interest of the estimation of absorbed dose to the liver arises. The liver, which because of new treatment techniques, has become a dose limiting organ in radionuclide therapies. The liver has a maximum tolerable dose (MTD) of about 35 Gy, based on early tissue reactions after external radiation therapy, published by Emami *et al.* [17] in 1991. The use of these data in radionuclide therapy is questionable, since they are based on an even irradiation field with a high dose rate resulting in the delivering of a uniform absorbed dose to the tissue, criteria not met for radionuclide therapies, due to heterogeneous distribution of the radiopharmaceuticals with lower dose rates. For radionuclide therapy, a requirement for the assessment of an absorbed dose level will require a calculation of the absorbed dose to parts of an organ, or at the cellular or subcellular level.

Most suitable for a situation similar to the one above, would be to create a small-scale dosimetry model of the liver tissue. By including the microstructures specific for the hepatic tissue and especially structures of known relevance in radionuclide therapy, the non-uniform distribution of radiopharmaceuticals could be taken into account and a more accurate estimate of the relevant absorbed dose could be made.

1.2 Aim

The aim of this master project was to develop a small-scale dosimetry model for a detailed and more accurate absorbed dose calculation on the scale of the hepatic microstructure.

Considering the heterogeneous distribution and concentration of radiopharmaceuticals within the liver tissue, absorbed doses to different source-target combinations will be calculated and discussed. The determination of the different source-target combinations was made through a literature search, searching information of microstructures plausible for radioactivity accumulation and microstructures reasonable to become target structures. The microstructural, and for possible future applications, also the subcellular distribution of radionuclides and radiopharmaceuticals are of great interest for this new approach of dosimetry calculations with applications in radiation protection, both inside and outside the clinical use of radionuclides.

The challenge for nuclear medicine during the 21st century will, according to ICRU Report No 67; *Absorbed dose specification in nuclear medicine* [18] be to present a dosimetry and a prediction of the biological effect due to the non-uniform distribution of radiopharmaceuticals caused, inter alia by the capability of targeting radionuclides to *i.e.* specific sites of a cell or to cell populations within an organ.

Therefore, taking the heterogeneous activity concentration into consideration, absorbed doses, both cross doses and self doses, to different source-target combinations will be calculated whereupon this small-scale dosimetry model may be useful in the discussion about the dose limit of the liver tissue used for today's radionuclide therapies.

2 Theory

The chapter covering the theory will in this thesis contain three main parts; one covering the morphology and pathology of the liver tissue, the second covering the theory concerning internal dosimetry and the MIRD-formalism and the third part containing the basics concerning the Monte Carlo method used for the absorbed dose calculations.

2.1 The liver

2.1.1 Macroanatomy of the liver

The liver is the largest solid organ of the body and the second largest organ after the skin. The weight of the liver is 1,5-2 kg and represents about 2% of the total body weight of an adult human and it is situated in the upper right quadrant of the abdominal cavity beneath the diaphragm. The liver is an interface between the digestive system and the blood. In fact all nutrients resulting from the digestion of the food that is taken up by the intestines are then processed by the liver for use by other parts of the body. In the circulation system the liver is located at an optimal position to gather, transform and accumulate metabolites from the blood from the intestines and for eliminating or neutralizing toxic substances [19]. The functions of the liver are numerous, besides the detoxification of drugs and toxins, also synthesis of many proteins (such as albumin, coagulations factors and enzymes), glycogen storage and release, metabolism of lipoproteins, formation and excretion of bile and many more, too numerous to list [9].

The bile production, performed by the liver cells by uptake, transformation and excretion of blood components into the bile canaliculi, is an exocrine[1] function of the liver. Stored in the gall bladder and released into the duodenum after a meal, the bile has an important function by emulsifying lipids in the digestive tract, by providing lipases, enzymes essential in the role of digestion and processing of dietary lipids[19].

Most of the blood (70-80%) in the liver comes from the portal vein arising from the stomach, intestines and spleen and the rest (20-30%) is supplied by the hepatic artery, branching from the aorta. The blood from the portal vein is nutrient-rich and oxygen-poor, whereas the blood from the hepatic artery is oxygen-rich [19].

2.1.2 Microanatomy of the liver

A functional subunit of an organ can be described as the smallest, structurally distinct unit that is capable of exerting all the organs functions autonomously. The definition of the hepatic structural and functional unit has been a topic of discussion all since the first description of a classic liver lobule, made by Kiernan in 1833 [20]. He described the functional unit as a hexagonal structure, the hepatic lobule, which until today remains the standard by which hepatic microarchitecture is named [9]. Thus should one be aware of that the debate regarding the hepatic functional unit until now has generated many models, but so far there is no final consensus. The liver is an inseparable continuum and all attempts to describe separate entities are artificial [21], so the one described below.

The hepatic lobule ($\sim 0{,}7 \times 2\ mm$) [19], see figure 2.1, consists mainly of the liver cells, *hepatocytes*, which are epithelial cells grouped into interconnected plates. Each hexagonal lobule has three to six *portal tracts* at its periphery, containing a portal vein, a hepatic artery and a bile duct [9]. Also present in the portal tracts is nerve fibers and lymphatic vessels

[1] Exocrine glands secrete their products into ducts that lead directly into the external environment.

[22]. In the center of the lobule there is the hepatic vein, hence called the *central vein* (CV) [9].

The blood supply of the hepatic lobule arises mainly, as mentioned in section 2.1.1 above, from the portal vein which branches repeatedly to smaller portal venules in the portal tract. The portal venules then branch into even smaller distributing venules that run around the lobule and lead the nutrient-rich blood into the sinusoids. The sinusoids are small blood vessels, similar to capillaries, but with fenestrated endothelium that runs radially towards the center of the lobule, where they converge to create the central vein. The sinusoids have an average diameter of 7 μm, since they show heterogeneity in the hepatic lobule. In the portal tracts the sinusoids are more tortuous in contrast to the sinusoids closer to the centrilobular regions where they appear straighter. A more detailed description of the sinusoidal diameter is found in review article by Braet *et al.* [23]; the diameter of the sinusoids near the portal fields measures 5,9 μm and the sinusoids in the centrilobular region measures 7,1 μm.

The hepatic artery branches repeatedly and form arterioles in the portal tracts, which add oxygen-rich blood to the sinusoids. Therefore blood always flow from the periphery of each lobule, to its center. The central venules from each lobule converge into veins, which form two or more large hepatic veins which empty into the *inferior vena cava* [9].

The interlobular bile network is supplied with bile produced by the hepatocytes. The hepatocytes also give rise to the intrahepatic bile network, since where two or more hepatocytes abut, they define a tubular space between them that is called the *bile canaliculi*. The bile canaliculi are the first part of the bile duct system, which terminates in the portal tracts, where the canaliculi empty into the bile ducts which gradually enlarge and form the left and right hepatic duct, which later on will leave the liver. Therefore the flow of bile in the hepatic lobule is opposite that of the blood [19].

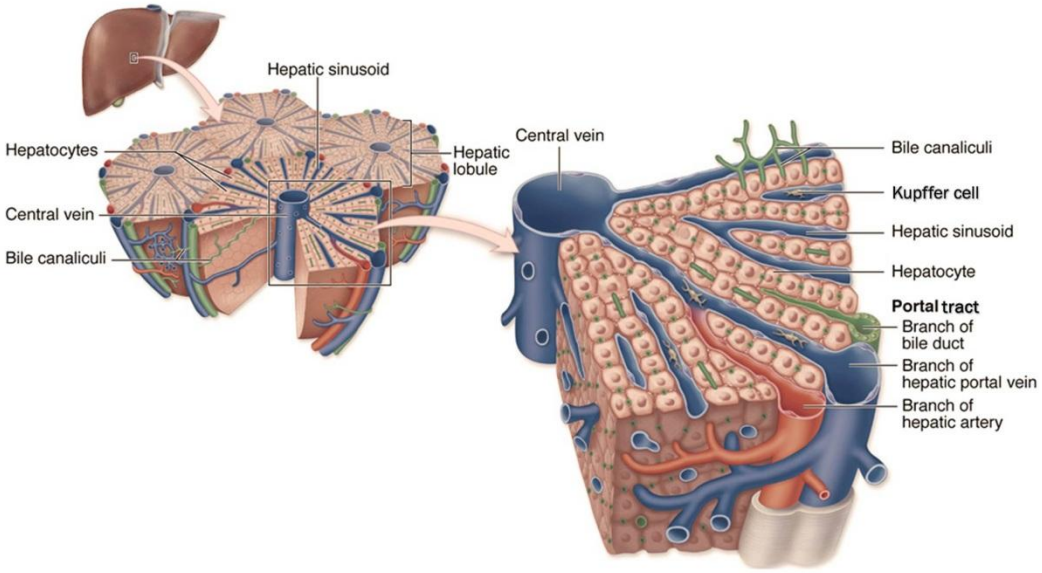

Figure 2.1. A sketch over the liver and the hepatic microstructures. The leftmost part of the figure shows the shape of the organ, whereas the middle part of the figure shows the division of the hepatic tissue into hepatic lobules, the structural and functional unit of the liver. The rightmost part of the figure shows, in more detail, the main microstructures of which the hepatic lobule consists of. Picture from [19], page 289.

One should keep in mind that the representation of the liver lobule is an artificial way of representing and describing the continuous organ, but it is justified since it is of great help when used for further understanding of pathophysiologic processes as well as for dosimetric calculations, like the one in your hand. Interesting is, that in some animals, *e.g.* pigs, one lobule are separated from another by a layer of connective tissue, making them easy to distinguish. The human liver contains much less connective tissue, giving the organ a much more continuous morphology [9], see figure 2.2 below.

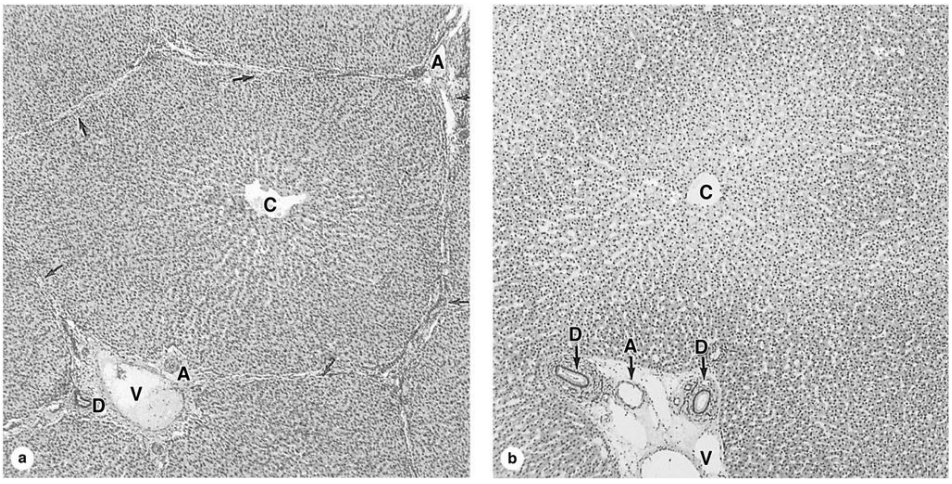

Figure 2.2. The hepatic lobule of **(a)** a pig and and **(b)** a human. The hepatic lobule of the pig is delimited at all sides of connective tissue, while the human hepatic lobule has much less connective tissue and the boundaries of the lobule are much more difficult to distinguish. The pictures also show the central vein **(C)**, the portal artery **(A)**, the portal vein **(V)** and the small bile ducts **(D)**. Picture from chapter 16, Organs associated with the digestive tract [19], page 289.

A consequence of the direction of blood flow in the sinusoids is that oxygen and metabolites, as well as all other toxic or nontoxic substances, first will reach the lobule's peripheral cells and then the more central cells. Hepatocytes near the portal areas can therefore rely on aerobic metabolism while the more central cells are exposed to lower concentrations of nutrients and oxygen [9].

Based on this knowledge of the hepatic microcirculation the classical lobules sometimes are subdivided into smaller functional units called liver acinus. This concept was first defined by Rappaport *et al.* in 1954 [24] and is important in describing some structural – functional relationships of the hepatic lobule. The liver acinus concept takes into account the gradient of oxygen and nutrition concentration along the sinusoids. In this formulation the portal tracts are at one point of the base of an isosceles triangle and the central vein at the sharp apex of the same triangle, thus each portal tract are supplying two or more classical lobule with oxygen- and nutrient-rich blood, see figure 2.3. A comparison of roughly equal terms of the classical lobule and the liver acinus is presented in table 2.1. The activity of each hepatocyte is determined by its position along this oxygen-nutrient gradient, which gives rise to three zones; zone 1, zone 2 and zone 3. Zone 1 is the most oxygen- and nutrient-rich zone which has a metabolic activity different from the one in zone 3, which is exposed to the lowest concentrations of oxygen and nutrition [9]. Many pathologic changes of the liver are best understood by the concept of the liver acinus [19].

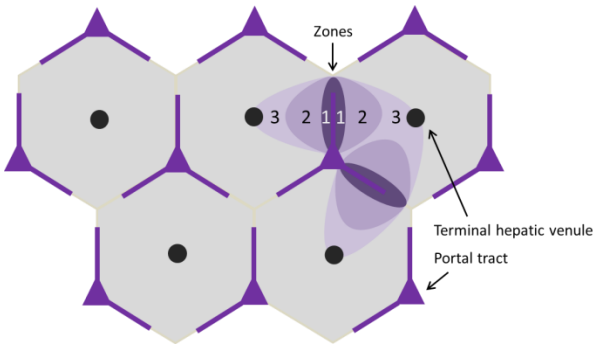

Figure 2.3. The concept of the liver acinus may be used to describe some structural-functional relationships in the hepatic lobule, due to its microcirculation giving rise to three zones; zone 1, zone 2 and zone 3 of in-zone equal blood pressure, oxygen content and concentrations of other characteristics. Figure layout inspired by [25].

Table 2.1. Comparison of approximately equal terms of the Kiernan's classical lobule and Rappaport's liver acinus.

Classical lobule	**Liver acinus**
Central vein	Terminal hepatic venule
Lobular center	Zone 3 ($\downarrow O_2, \downarrow nutrition$)
Midlobular	Zone 2
Lobular periphery	Zone 1 ($\uparrow O_2, \uparrow nutrition$)

2.1.3 Cell types of the liver

The liver cells, the *hepatocytes*, are epithelial cells that are grouped into interconnected plates arranged into thousands of roughly hexagonal hepatic lobules, which are the classical structural and functional unit of the liver. In the lobule the plates of hepatocytes are arranged radially around the central vein, branching towards the periphery of the lobule forming a sponge-like structure [19]. Approximately 78 % of volume of the hepatic lobule is made up of hepatocytes and about 60 % of the amount of cells [21].

The hepatocytes are large polyhedral cells with six or more surfaces. Their typical diameter is 20-40 μm [9, 19]. The hepatocytes have large circular nucleus, which is common in cells very active in protein synthesis and in the adult man 25 % of the hepatocytes are binucleate, *i.e.* having two nuclei [9]. Other constellations of multiple nuclei, with four or eight time the normal diploid chromosome number are also common [19].

The hepatocytes have three kinds of plasma membranes, one for each kind of contact surface, since one hepatocyte always is in contact with blood, bile and other hepatocytes, see figure 2.4 below. The surface in closest contact with the blood is the *sinusoidal*, facing the sinusoid. The surface in contact with bile is the *canalicular*, facing the bile canaliculi and the surface in contact with the adjacent hepatocytes is the *lateral*, facing intercellular space between hepatocytes. The direction of transport of substances in the hepatocytes is from the sinusoidal surface to the canalicular surface, *i.e.* from the blood to the bile.

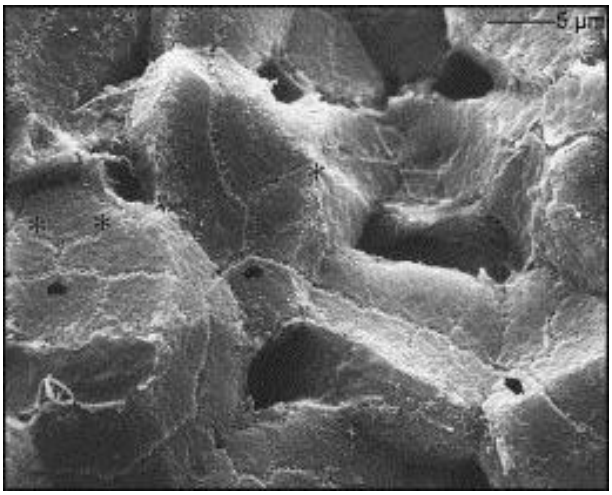

Figure 2.4. Scanning electron micrograph (SEM) picture showing a number of neighboring hepatocytes and their different plasma membranes, facing the sinusoids, the bile canaliculi and the adjacent hepatocytes, *i.e.* each hepatocyte is in contact with blood, bile and other hepatocytes. The small canals are the bile canaliculi, bifurcations indicated by arrows (➘) in the figure and blunt ends by asterisks (*), transporting the bile produced by the hepatocytes to the bile ducts in the portal fields. The dimension of the picture is indicated by the scale bar in the upper right corner. Picture reprinted with permission from [9], page 15.

The hepatocyte surface in contact with the bile is the *canalicular*, which is facing the bile canaliculi. The canaliculi, which are the first portion of the bile duct system, are small long spaces approximately 1 µm in diameter [19], thus varying form 0,5-1 µm near the lobular center in zone 3 to 1-2,5 µm in the portal tract [9].

The lateral surface, facing intercellular space between hepatocytes, extends from the margin of the bile canaliculi to the sinusoidal surface and is specialized for cell attachment and cell-cell communication.

The sinusoidal membrane of the hepatocytes, the one in closest contact with the blood, is facing the perisinusoidal *space of Disse*, a small space 0,2-0,5 µm wide located between the hepatocytes and the endothelial sinusoidal cells [21]. The sinusoidal endothelium consists of a layer of fenestrated endothelial cells, see figure 2.5 below. The fenestrae, often grouped together, measures 150-175 nm and occupies around 6-8% of the endothelial surface. The grouped fenestrae acts as a dynamic filter for particles in the plasma, therefore filtering solids, solutes and particles small enough to pass the fenestrae, enter the space of Disse and reach the hepatocytes [23], or the hepatocyte microvilli projected into the space of Disse which may be of importance to keep the space open [9]. Lager molecules, like erythrocytes and macromolecules have diameters larger than the sinusoidal fenestrae (erythrocytes have a diameter of approximately 7,5 µm [19]), won't pass through the fenestration and will not enter the space of Disse. Instead, the microvilli on the hepatocytes sinusoidal surface project into the space of Disse and in to the sinusoidal lumen. This will approximately increase the absorptive and secretive activity six times [9] and the construction gives rise to a two way exchange, the key function of the liver; between macromolecules, like lipoproteins and albumin, secreted to the blood by the hepatocytes and on the other hand macromolecule taken up from the blood up by the hepatocytes to be catabolized [19].

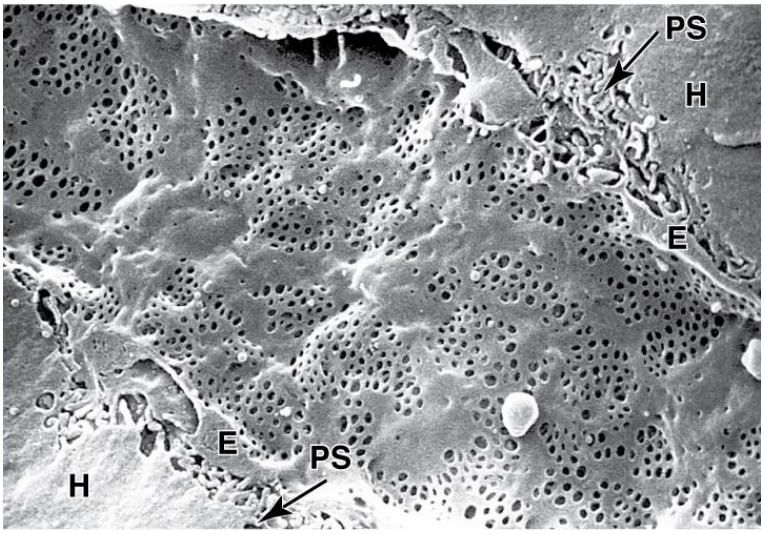

Figure 2.5. Scanning electron micrograph (SEM) picture of the fenestrated sinusoidal endothelium surface. In the upper right and lower left corner edges of hepatocytes (**H**) are seen. The perisinusoidal space (**PS**), *space of Disse* where the microvilli of the sinusoidal are projected, is seen between the hepatocyte surface and the endothelial cells (**E**) of the sinusoid. X6500. Picture from *Junqueira's Basic Histology* [19], page 292.

The liver is the largest, single source producer of lymph in the body, producing 15-20% of the overall volume. The function of the lymph is to drain the interstitial spaces of an organ from excess fluids and proteins. The interstitial space of Disse is assumed to be where the hepatic lymph mainly is formed, but with a complement associated with the small branches of the intrahepatic lymphatic tree found in the portal tract. The route followed by the produced lymph has long been discussed, since no lymphatic capillaries are found within the parenchyma and there are no direct channels between the space of Disse and the primary lymphatics and it has therefore been suggested that "endothelial massage" by blood cells in the sinusoids is responsible for the transport of lymph. The endothelial massage appears since the diameter of both the erythrocytes and the white blood cells exceeds the diameter of the sinusoid. The erythrocytes are quite flexible and can easily bend to pass through small capillaries [19], but the white blood cells are less plastic and do not easily adapt to changes of capillary diameter, thus resulting in a pressure on the space of Disse causing fluids in the space to be pushed down stream and when reaching a fenestrae the fluid will be pushed out of the Space of Disse [23]. The consequence of this is assumed to be a retrograde fluid movement in the Space of Disse, transporting the lymphatics towards the portal tracts, since movement of fluorescently-labeled lymphocytes have been observed to be in that direction [9]. At the periphery of each lobule, at the portal tracts, the lymphatics leave through gaps between the hepatocytes, either along blood vessels penetration the limiting plane or independently of blood vessels. The fluid then enters into portal tracts lymphatic vessel, travelling down the portal tree exiting though the lymphatic vessels in *porta hepatis*.

Associated with the hepatic sinusoids are two noteworthy cells; the hepatic macrophages called Kupffer cells and the fat storing hepatic stellate cells. The hepatic stellate cells, previously often called Ito cells, are found in the space of Disse and contain many small lipid droplets, rich in vitamin A, making them fat storing cells [9].

The other cell mentioned above is the Kupffer cell. Kupffer cells are liver specific macrophage, belonging to the mononuclear phagocytic system (previously classified as the reticuloendothelial system (RES)), and are found in the lumen of the sinusoids throughout the liver, see figure 2.6 below. The Kupffer cells have been considered to be fixed cells in the sinusoidal membrane, but in fact they are capable of migrating along the sinusoids, both with and against the blood flow and they also have the capability of migrating into areas of liver injury and into regional lymph nodes [9].

The most important Kupffer cell function is the uptake and processing of particulate and soluble material from the blood entering the hepatic lobule in the portal tracts. The Kupffer cells make up the first macrophage population of the body to blood originating from the gastrointestinal tracts and are the first macrophages to come in contact with *e.g.* bacteria and bacterial endotoxins originating from the intestines. As macrophages they are capable of phagocytosing foreign material, scavenging[2] microorganisms and degrade effete erythrocytes and circulating tumor cells [9].

The life span of the Kupffer cells averages several months and they are, at least in part, renewed by transformation of circulating monocytes, which migrate to the liver. Still some self-renewal, though limited, occurs through cell division even though the mitotic index and the proliferation rate of the Kupffer cells are low [21].

The Kupffer cells have an irregular stellate shape, with a size hard to define due to its shape. Since the Kupffer cells are resting on the endothelial lining of the sinusoid lumen, their size cannot exceed the diameter of the sinusoid, approximately 7 μm [9, 23], in more than one direction. The Kupffer cells are also associated with the existence of microvilli projecting at the cell surface, making their size even harder to define [9].

The Kupffer cells are not evenly distributed throughout the hepatic lobule, but are more numerous in the periportal region [9]. Forty-three percent of the Kupffer cells are found in the periportal zone 1, 32% in zone 2 and 25% in perivenous zone 3 [21]. They also show a functional heterogeneity in the lobule, where the Kupffer cells in the periportal region are larger and are more active in phagocytosis than the Kupffer cells in the perivenous area [9], due to the directions of blood flow through the hepatic lobule.

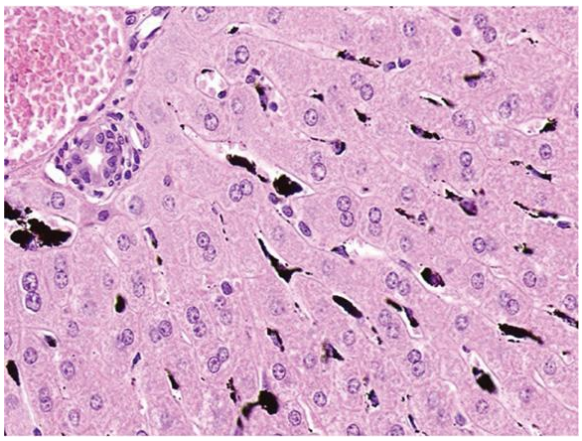

Figure 2.6. Kupffer cells, found in the endothelial lumen of the sinusoids, seen in a rat liver injected with particulate India in as black cells in the part of a lobule above. X200. Picture from *Junqueira's Basic Histology* [19], page 291.

[2] Scavenging is both a carnivorous and herbivorous feeding behavior in which the scavenger feeds on dead and decaying organic matter.

In table 2.2 below a summary of the microstructures and the cell types discussed above can be seen.

Table 2.2 Glossary and summary of microarchitectural terms.

Hepatic lobule	The classical hexagonal lobule first defined by Kiernan in 1833, considered to be the structural and functional unit of the liver.
Central vein	Placed at the center of each hepatic lobule, where it receives blood from the sinusoids and returns it to the circulatory system via the hepatic vein.
Portal tract	The periphery of each lobule is delimited by portal tracts, containing a portal vein, a hepatic artery and a bile duct.
Portal vein	A branch of the hepatic vein, forming these venules in the portal tracts. The portal vein is the input of nutrient rich blood in the lobule.
Portal artery	A branch of the hepatic artery, forming these arterioles in the portal tracts. The portal artery is the input of oxygen rich blood in the lobule.
Bile duct	A branch of the bile network, receiving bile from the bile canaliculi for further transportation to the gall bladder.
Sinusoids	Small blood vessels, similar to capillaries, but with fenestrated endothelium that runs radially towards the center of the lobule, where they converge to form the CV.
Bile canaliculi	The intrahepatic bile network, defined by the tubular space between two or more adjacent hepatocytes. The bile canaliculi transports the bile produced by the hepatocytes towards the bile duct in the portal tract.
Space of Disse	A small space between the sinusoids and the hepatocyte important for the exchange of substances between the hepatocytes and the blood in the sinusoidal lumen. The space of Disse is also assumed to be the main structure producing the hepatic lymph.
Kupffer cells	The Kupffer cells are the liver specific phagocytic macrophages partially stationary in the lumen of the sinusoids of the liver.

2.1.4 Composition of the liver lobule

The composition of the liver lobule is mainly out of the different cell types and microstructures mentioned above. Interesting for the aim of this project, to design and create a model of the hepatic lobule, which than will build the whole organ The morphometric composition of the liver lobule, presented by Dancygier [21] is described in table 2.3 underneath. The volume densities of mentioned cell types or compartments are calculated regardless of blood and bile contents.

Table 2.3. Morphometric composition of the liver lobule [21].

Cell type/compartment	**Volume density (%)**
Hepatocytes	77,7
Non-hepatocytes	6,3
Sinusoidal space	2,8
Kupffer cells	2,1
Stellate (Ito) cells	1,4
Extracellular space	16

In addition to the cell types of the liver, also the blood and bile fractions of the liver are of interest for the aim of this project. According to section 7.7.2 in the ICRP Publication 89 [26]; *Basic Anatomical and Physiological Data for Use in Radiological Protection: Reference Values*, which gives the reference values for the regional blood volume and blood flow rates in organs and tissue in adults, the blood content in the liver in percent of the total blood volume, is 10 % for both male and female.

The reference value of the total blood volume is also stated in the above mentioned publication, ICRP Publication 89, in table 2.11 in section 2.2.1. The total blood volume for males is 5300 ml and for females is 3900 ml. Also found in the publication, in table 2.8, is the reference values of organs and tissues as a function of age, where stated is that the adult male liver has a mass of 1800 g and the adult female liver has a mass of 1400 g.

Table B.1 in annex B in ICRP Publication 110; *Realistic reference phantoms: an ICRP/ICRU joint effort. A report of adult reference computational phantoms [27]*, which lists all the mediums, densities and masses of each organ and tissue used in the reference adult male and female phantom, gives the blood density 1,060 g/cm^3.

Merging this information gives the blood volume in the average liver as a percentage of the total liver mass, see table 2.4 below:

Table 2.4. Table containing the calculation of the average blood percentage of the liver. Density of blood from [27]

Average $\frac{♂+♀}{2}$ blood volume in the liver:	$= 10\,\% \cdot \frac{(5300\ ml\ + 3900\ ml)}{2} = 460\ ml$
Average $\frac{♂+♀}{2}$ mass of blood in the liver:	$= \left[\rho = \frac{1{,}06\ g}{cm^3}\right] = 460\ ml\ \cdot 1{,}06 \frac{g}{ml} = 487{,}6\ g$
Average $\frac{♂+♀}{2}$ mass of the liver:	$= \frac{(1800\ g + 1400\ g)}{2} = 1600\ g$
Average $\frac{♂+♀}{2}$ blood percentage in the liver:	$= \frac{487{,}6g}{1600g} = 30{,}5\%$

The total volume of the human biliary system was quantitatively calculated by Ludwig *et al.* in 1998 [28], using computer-aided three-dimensional imaging techniques. Detailed measurements were made on three autopsy livers, with weights 1710 g, 2015 g and 2600 g, which by gravity infusion from a syringe connected to the hepatic duct, were filled by a contrast agent containing barium sulfate. Computer tomography (CT) images of the three livers were taken from which 3D images of the biliary tree were created. The volume of the infused contrast medium, representing the biliary tree, was quantified by summing up all brightness values exceeding an appropriate threshold value. These macroscopic measurements resulted in an average biliary tree volume of 20,4 cm^3.

Ludwig *et al.* also performed some microscopic measurements of the biliary tree, by studying computer generated 3D images of microscopic bile ducts, from a serially sectioned paraffin block from a normal liver. The microscopic bile duct in the studied portal tract, represented approximately 2,7 % of the portal tract volume.

Combining these calculations, the macroscopic and the microscopic, were the microscopic measurements from the block were applied to the whole liver, suggesting that the microscopic bile ducts would represent about 40 % of the hepatic duct system, the total volume of the bile ducts in the liver would be 29 cm^3. It should be notes though, that the authors are aware of the reduction of accuracy in the measurements when applying the microscopic measurements to the entire liver. Attention should also be paid to the fact that no attentions was paid to the volume of the bile canaliculi existing throughout the lobule.

The density of the bile is assumed to equate to the density of the gall bladder content, listed in table A.1 in annex A in ICRP Publication 110 [27], stated to be 1,030 g/cm^3. This, combined with the information about the hepatic bile volume calculated by Ludwig et.al, gives the percentage of bile in the liver, see table 2.5:

Table 2.5. Table containing the calculation of the average bile percentage of the liver. Density of bile from [27].

Average volume of bile in the liver [28]:	$= 29\ cm^3$
Average mass of bile in the liver:	$= \left[\rho = \frac{1{,}030g}{cm^3}\right] = 29\ cm^3 \cdot 1{,}030\frac{g}{cm^3} = 29{,}9g$
Average percentage of bile in the liver:	$= \frac{29{,}9g}{\left(\frac{1710+2050+2600}{3}\right)g} = 1{,}4\%$

If taking into account the blood and bile volume of the liver and applying the morphometric composition of the hepatic lobule to the entire liver, the composition of the liver would be, the one presented in table 2.6.

Table 2.6. Composition of the liver, divided into percentage of cell type and compartment.

Cell type/compartment	**Volume density (%)**
Blood	30,5
Bile	1,4
Hepatocytes	53
Non-hepatocytes	4,2
Sinusoidal space	1,9
Kupffer cells	1,4
Stellate (Ito) cells	0.9
Extracellular space	10,9

In table 2.7 a summary of the dimensions of the microarchitectural structures are presented, dimensions that later on will be implemented in the small-scale dosimetry model created.

Table 2.7. Approximate dimensions of microarchitectural structures in the hepatic lobule. Dimensions which will be used in the small-scale dosimetry model created.

Length of the edge of a lobule	500 µm (derived from the approximate size of the hepatic lobule ($\sim 0{,}7\ x\ 2\ mm$))	[19]
Height of a lobule	2 mm	[19]
Diameter of central vein	70 µm	[9]
Diameter of portal vein	30 µm	[9]
Diameter of portal artery	10 µm	[9]
Diameter of portal bile ducts	20 µm	[21]
Diameter of sinusoids	7 µm	[23]
Width of Space of Disse	0.5µm	[9]
Width of bile canaliculi	1-2 µm	[9]
Size of hepatocytes	Approximately 30 µm. Will be defined as a 25 µm thick slice of a hexagon with the edge length of 33 µm.	[9, 19]
Size of Kupffer cells	Hard to define due to its shape, but could be defined as an ellipsoid where two axes cannot exceed the dimension of the sinusoid, whereas the major axes can extent along the sinusoids. Chosen length of major axis is 16 µm.	

2.1.5 Hepatic toxicity from ionizing radiation

The hepatic toxicity from radionuclide therapy is, due to the accumulation and transport of radionuclides thought to be related to the microarchitecture of the hepatic lobule, even though the tolerance dose (TD) used as an absorbed dose limit of the liver tissue today is based on pathological and clinical studies from external whole liver irradiation.

In the 1960s some pathological studies demonstrated the incidence of hepatic lesions after radiation therapy to the abdominal region [22]. Reed and Cox [29], who in 1965 published their record of the pathology of 12 patients delivered in total 30-59 Gy to the liver by a linear accelerator over a period of six weeks with five fractions a week. They thereafter described the pathology of these patients and established the features of radiation induced liver disease (RILD).

The anatomical substratum of RILD is the veno-occlusive disease (VOD), which is characterized by centrilobular congestion. On a microscopic level, the characteristics are a severe congestion of the central vein and of the sinusoids near the center of a lobule, a severity decreasing towards the portal tracts. Around the central parts of each lobule there is atrophy[3] and many of the hepatocytes in close vicinity of the central vein is absent. The central vein on the other hand is usually quite hard to recognize, since the vessel lumen is occupied by a fine criss-cross network of collagen fibrils, emanating from the endothelial cells facing the lumen. Numerous erythrocytes could be found trapped in the network, in severe cases leading to necrosis in the center of affected areas and the collapse of entire lobules. Also in adjacent sinusoids the crisscrossing fibril network can be found. In the portal tracts a mild congestion can be found, but in comparison to the change in the central parts of the lobule, the portal tracts appear almost normal. The change of the veins dose not only occur to the central vein, but also to the sublobular veins, but in contrast the larger veins as *vena cava* do not show any signs of VOD [22].

The pathogenesis of RILD has however not fully been described since there, in 2001 was a lack of an appropriate animal model and no experimental animal have so far produced RILD by irradiation alone. A combination of radiation and chemotherapy in dogs has been able to produce VOD, but then with the difficulty to determine the contribution from the two individual agents. This has prevented the definition of the actual target of radiation within the liver tissue [22]. But, since the anatomical substratum of RILD is the VOD, the main structures at risk in the hepatic tissue seems to be the endothelial cells in the central and sublobular veins and in the terminal portion of the sinusoids [22]. Evidence from electron microscopy studies of patients who died of VOD also points in the direction that the target of fatal damage would be the endothelial cells in areas around the central veins and the adjacent sinusoids [22, 30]. Most likely the hepatocytes is not the main target, but they become secondarily affected, because of the loss of vascular access, leading to necrosis and fibrosis from anoxia [22].

In addition to the description of RILD, the paper published by Reed and Cox [29] resulted in the opinion concerning the tolerance dose for the liver to be 30-35 Gy, if the tissue was irradiated with a conventional fractional scheme. In 1991, data was summarized in a publication from Emami *et al.* [17], concerning the MTD of different organs, among others the liver. Data, obtained from an extensive literature search, was presented as tolerance doses (TD) for the 5 % risk of complications within five years (TD5/5) and the 50 % risk of complications within 5 years (TD50/5), reported as a function of the volume of the normal tissue irradiated (1/3, 2/3 or the total volume). The TD5/5 for a 1/3

[3] Atrophy is the general physiologic process of reabsorption of tissue; on a cellular level involving apoptosis if caused by natural causes.

irradiated liver is 50 Gy, 2/3 irradiation is 35 Gy and the TD5/5 for a 3/3 irradiated liver is 30 Gy, whereas the TD50/5 for 1/3 irradiation is 55 Gy and for a 3/3 irradiated liver the TD50/5 is 40 Gy.

In 2005 Welsh *et al.* [31] summarizes some from publications concerning the tolerance of the liver tissue. The liver tolerance was seen to be significantly increased for a partial rather than a whole liver irradiation. When only one third of the liver was irradiated, the TD50 could increase to as high as 67 Gy. For SIRT treatments the locally absorbed liver doses often exceeds 50 Gy, but could possibly be as high as 150 Gy. With the normal tissue complication level, derived from external whole volume irradiation, a significant amount of RILD would have been expected. Yet complications are rare. The explanation is considered to be the heterogeneous distribution of the microspheres within the liver, giving a very high locally absorbed dose and a high tumor-to-normal tissue absorbed dose ratio.
In 2004, Kennedy *et al.* [30] presented an analysis of the distribution within the liver microstucture of resin or glass ^{90}Y-microshperes used for SIRT-treatments. They showed that just a few microspheres were to be found in the portal veins, since nearly all spheres were found in the small- to medium sized arteries with a diameter of 12-30 μm, typical dimensions for the portal artery, all according to the theory behind the treatment technique; the microspheres are injected into the hepatic artery since it is assumed that metastatic lesions in the liver almost exclusively receives blood supply from the hepatic artery. In contrast, the blood supply of the normal liver tissue primarily is derived from the portal vein [31]. This natural difference in blood supply derives a higher flow of microspheres in the peri- and intra-tumoral arterial vasculature [31].

These indications; that an increasing inhomogeneous irradiation of the liver tissue leads to a higher tolerance dose, indicates that the absorbed dose limit from external, whole body irradiation may not be applicable to radionuclide therapies, where the irradiation field and the energy absorption in many cases become extremely heterogeneous.

2.2 Internal dosimetry

The absorbed dose is a measurable quantity of the energy deposited in a medium originating from ionizing radiation. Absorbed dose, D, is defined as the quotient of $d\bar{\varepsilon}$ by dm, where the $d\bar{\varepsilon}$ is the mean energy imparted, where the energy imparted, ε, is the sum of all energy deposits in a volume and dm the mass of the matter. Absorbed dose is expressed in the unit Gy [J/kg] [32].

$$D = \frac{d\bar{\varepsilon}}{dm} \qquad \text{Eq. 2.2.1}$$

Internal absorbed doses, received by a patient by radioactively labeled drugs in medical use, which by infusion or by oral intake resides inside the body, are calculated to ensure the safety of the patients and to guarantee the prescribed absorbed dose to the treatment area. This is called internal dosimetry, and in contrast to the absorbed doses measured or calculated from external radiations sources, internal doses can never be directly measured. Instead some standard procedure for dose calculation, based on assumptions, must be made. Some methodologies exist for the calculation of mean absorbed doses from internal emitters in nuclear medicine and the formalism normally used is established by the Medical Internal Radiation Dose (MIRD) Committee of the Society of Nuclear Medicine [33].

2.2.1 The MIRD formalism

The MIRD Committee provides a technique, equations and other resources needed for the calculation of mean internal dose calculations. This guidance is called the MIRD formalism [1], and can be summarized as follows.

The mean absorbed dose rate to a target organ or structure, assumed to have a homogeneous atomic composition and a uniform mass density, from a source structure also assumed to have a uniform mass density and atomic composition, as well as a homogeneous distribution of activity, is given by:

$$\dot{D}(r_T \leftarrow r_S, t) = A(r_S, t) \cdot S(r_T \leftarrow r_S, t) \qquad \text{Eq. 2.2.2}$$

Equation 2.2.2 is an expression for the time dependent mean dose rate, $\dot{D}$ at the time t, to the target region r_T, from the source region r_S. The mean dose rate, $\dot{D}$,is the product of the time dependent activity in the source region $A(r_S, t)$ and the dose conversion factor, $S(r_T \leftarrow r_S, t)$ called the S-factor, specific for any type of radiation, energy and source-target combination.

The absorbed dose to a target region r_T can be divided into two contributing parts, see below. The contribution from each of these parts is of great value in situations when the origin of each absorbed dose contribution to the target region r_T is of interest.

(I) *Self-dose*; the absorbed dose originating from energy emitted and absorbed in the source region itself $(r_T = r_S)$.
(II) *Cross-dose*; the absorbed dose in target region originating from energy emitted from surrounding sources $(r_T \neq r_S)$.

The mean absorbed dose in the target region r_T at the time T_D after the injection of the radioactive material is the sum of all contributions from the contributing source regions, obtained through a dose-integration expressed as follows:

$$D(r_T, T_D) = \int_0^{T_D} \dot{D}(r_T, t)dt = \sum_{r_S} \int_0^{T_D} A\,(r_S, t) \cdot S(r_T \leftarrow r_S, t)dt \qquad \text{Eq. 2.2.3}$$

The above equations, [2.2.2: 2.2.3] describe the time-dependent MIRD formulation, a formulation needed if the area of interest for absorbed dose calculation is increasing or decreasing during the period of irradiation. In most of cases the masses of both source and target area remain constant during the period of irradiation and the time-dependency of the S-factor therefore can be ignored, [1], resulting in the following alteration of Eq. 2.2.3:

$$D(r_T, T_D) = \sum_{r_S} \tilde{A}(r_S, T_D) \cdot S(r_T \leftarrow r_S) \qquad \text{Eq. 2.2.4}$$

In equation 2.2.4 the absorbed dose expression is separated into the cumulated activity and the S-factor, where the cumulated (time-integrated) activity $\tilde{A}(r_S, T_D)$ in source region r_S over the dose-integration time $[0: T_D]$, which in other words gives the total number of nuclear transitions during that time, see Eq. 2.2.5 below:

$$\tilde{A}(r_S, T_D) = \int_0^{T_D} A\,(r_S, t)dt \qquad \text{Eq. 2.2.5}$$

The S-factor, representing the mean absorbed dose rate to target region r_T at the time t after injection per unit activity in source region r_S, is defined by:

$$S(r_T \leftarrow r_S) = \sum_i \frac{\Delta_i \cdot \phi_i(r_T \longleftarrow r_S)}{m_T} \qquad \text{Eq. 2.2.6}$$

Equations 2.2.6 containing Δ_i, the mean energy emitted per nuclear transition, in turn consisting of the product $y_i \cdot E_i = \Delta_i$, where y_i is the number of ith transitions per nuclear transformation and E_i is the mean energy of the ith transition. It is also containing the absorbed fraction, $\phi_i(r_T \longleftarrow r_S)$, the fraction of energy emitted from the source region, r_S that is absorbed in the target region r_T, for the ith component of the radioactive decay. For β-particles; if their range in tissue is short relative to the range of the target tissue, when defined as an organ, the absorbed fraction will be close to one. Thus the absorbed fraction for photons with ranges long compared to the range of the target tissue, the absorbed fraction will be less than one.

The product of Δ_i and $\phi_i(r_T \longleftarrow r_S)$, divided by the mass of the target region, m_T, this gives the S-factor. Therefore the S-factor is depending on the sex- and age-specific anatomical model chosen to represent the patient or organ of interest. The conventional S-values for specific organs may be based on computational whole-body phantoms representing reference individuals of a given sex, age and total body mass [27, 33].

The term arising when dividing the absorbed fraction with the mass of the target region, is called the specific absorbed fraction, $\Phi_i(r_T \longleftarrow r_S)$. The S-factor can thus be described as the product of the specific absorbed fraction and the mean energy emitted per nuclear transition, see equation 2.2.7 below

$$S(r_T \leftarrow r_S) = \sum_i \frac{\Delta_i \cdot \phi_i(r_T \longleftarrow r_S)}{m_T} = \sum_i \Delta_i \cdot \Phi_i(r_T \longleftarrow r_S) \qquad \text{Eq. 2.2.7}$$

The separation of equation 2.2.4 into cumulated activity and S-factors is convenient because the cumulated activities include the biokinetic properties of the radiopharmaceuticals, while the S-factors describe the energy deposition of the radionuclide in the target region, due to the physical properties of the emitted radiation in the source region, making the S-factor radionuclide specific, whereas the biokinetic parameter is radiopharmaceutical- and patient-specific.

The formulas in the MIRD formalism, described above, in combination with the computational whole-body phantoms [27, 33] also mentioned above, is a simplification of the complex nature of internal dosimetry. The phantoms used for absorbed dose calculations is created to meet the requirements of the uniform isotropic model; the organs inside are assumed to be large enough for edge effects to be negligible, the organs consist of a homogeneous material and that the activity is uniformly distributed with in each of the source regions.

For radionuclide therapies the conditions for the uniform isotropic model is known not to be satisfied, since the distribution of radiopharmaceuticals, intended or unintended, is known not to be uniform [3-7]. The MIRD formalism, used on a macroscopic scale, with target region represented by organs satisfying the uniform isotropic model, the formalism is not a good approach for the calculation of absorbed doses in radionuclide therapy.

On the other hand, the MIRD formalism is a general approach for the dosimetry of internal emitters and the formulation is applicable to arbitrary source and target regions, in any whole body-, organ-, multicellular-, cellular- or subcellular- model created, where its utility solely depends on its biological relevance [15]. The MIRD formalism itself is therefore valid as long as the source and target regions not are becoming too small that the statistical fluctuations of the decay and the energy deposition increases, since situation like that would require a microdosimetric approach [34].

2.2.2 Small-scale dosimetry

Small-scale dosimetry is an approach using the conventional MIRD formalism on dosimetric models where the source and target regions are of dimensions comparable to the length of emitted alpha particles, beta particles and low-energy electrons, which would allow for absorbed dose calculations on a scale comparable to the range of these particles. When using the conventional MIRD formalism on whole body phantoms [27, 33], charged particles are often considered to be locally absorbed in the source region itself, resulting in an absorbed fraction, $\phi_i(r_T \longleftarrow r_S)$ equals to one. However, when the source and target regions is of the size of a few millimeters or less, the range of the electrons will not be considered short compared to the length of the regions of interest and the assumption of the absorbed fractions equality to one no longer holds true [35].

The dimensions of structures in these small-scale dosimetry models is of great importance, since a change in distance between a source and target region of the length of a particle range could change the cross-dose (the absorbed dose in target region originating from energy emitted from surrounding sources) from significant to totally insignificant. The absorbed dose from emitted photons on the other hand are not that affected by a small increase of dimensions, since it will only result in a slightly increased attenuation and a small change in the solid angle of emission.

Small-scale dosimetry models, suitable for a heterogeneous radiopharmaceutical distribution does not imply that the uniform isotropic model or the concept of S-factors has to be abandoned. S-values can be calculated for multicellular, cellular or subcellular levels but the utility of the calculations will be limited by the biological input data; cellular dimensions, uptake and clearance pattern, fraction of labeled cells and the location of the radiopharmaceutical within the cell. Accordingly, an appropriate model together with a set of biokinetic data, the MIRD Schema with individual cells serving as "organs" and with the uniform isotropic model still valid, if now at the cellular scale, will still be suitable for absorbed dose calculations [15].

2.3 The Monte Carlo Method

The calculation of absorbed dose on a microstructure scale will require a full representation of the radiation emission, the radiation transport through the regions of interest defined within the tissue and the energy deposition in the in each of the individual microstructures.

The particle transport through a material is of a stochastic nature, even though it on a macroscopic scale often is depicted according to the exponential decrease, relating the absorption of light to the properties of the medium it is travelling through. A deterministic method will therefore solve the transport equation for the average particle behavior.

The full representation of every individual particle, which will be needed for absorbed dose calculations on a microstructural scale, will require a powerful simulation method recording the interaction and thus, if existing, absorption position of each emitted particle. This can be done by Monte Carlo (MC) simulations.

3 Material and methods

In this section the material and methods will be discussed. The material and method used is primarily a general-purpose Monte Carlo N-Particle code called MCNP[4] [36], which in some more detail will be described below.

3.1 The Monte Carlo method

Monte Carlo methods (MC) generate approximate solutions to mathematical problems by performing statistical sampling experiments. This gives the MC methods a great flexibility, much greater than any analytical method using a mathematical description for the input parameters in the problem. The MC methods can therefore be applied on problems with no probabilistic content as well as to problems whose inherent structure is probabilistic.

A MC method solves a specific problem by simulating the individual particles contributing to the endpoint of the problem by recording the feature of interest of their behavior. That feature of interest could be average flux over a surface, fission energy deposition averaged over a cell or energy distribution of pulses created in a physical detector. The average behavior of particles in a specific problem is in a MC method achieved by creating the average value of the all individually simulated particles, comparable to the results achieved by a deterministic method.

Monte Carlo methods involve a random sampling of the position of a radioactive decay, in a defined volume, and are thereafter capable of tracking the emitted particle or particles in a wide range of complex geometries [35]. The MC method is therefore suited for solving complex three-dimensional problems in allowing detailed representation of the feature of interest for all constituent particles in the problem.

The applications for MC transport codes are many and new fields are in constant developing. Some examples of today's applications are [37]:

- Research on accelerator-driven energy sources
- Design of the shielding in accelerator facilities
- Design of accelerator spallation targets for neutron scattering facilities
- Design of neutrino experiments
- Dosimetry calculations
- Different medical physics applications, including among others dose distribution calculations from proton and neutron therapies, as well as from radionuclide therapies, design and performance tests of detectors and correction methods for imaging techniques in nuclear medicine

The Monte Carlo methods are used to simulate a statistical process, such as the interaction of a particle with matter, by sequentially simulate all individual probabilistic events in the process. For the simulation to be carried out one must know what events that can occur and their individual probability, also known must be the environment where the process occurs. The physical process of interest must therefore be able to be expressed by a probability density function (pdf), a function describing the probability for a random variable to fall within a particular interval, a probability given by the integral over the interval of the pdf; giving the random variable's density over the region.

[4] **MCNP**, **MCNP5**, "**MCNP Version 5**" and **MCNPX** are trademarks of Los Alamos National Laboratory

By describing the physical process as a pdf, which has its origin in experimental data or a theoretical model describing the process, one can sample an outcome from the pdf, *i.e.* one has the opportunity to simulate the actual physical process. To be able to select stochastic samples from the pdf, the simulation is based on repeated random sampling, a sampling based on the selection of random numbers.

The random numbers used for the random sampling are needed for the selection among the different events that can occur in the process. A random sequence of numbers is generated using a random number generator; basically a function generating a sequence of numbers which seems to have been randomly sampled from a uniform distribution in the range [0:1], hence the generator often is called "pseudo-random-generator, since the sequence can be repeatable and the sequence will pass a statistical test for randomness [38].

Monte Carlo simulations sample the probability distribution for each variable of interest to perform on out of hundreds or thousands of possible outcomes, giving the probabilities for different outcomes to occur. For the estimate of the variable of interest to converge towards the accurate solution, a large number of histories need to be simulated. The accuracy of the estimation then depends on the correctness of the pdf's, the parameters set as the inputs of the model and the generation of random numbers used for the random sampling [34]. For a particle travelling through a medium, the MC method therefore are able to determine the most probable outcome at every step of the particles life [36].

The simulation approach for particle transport is based on modeling the particles collisions using physical equations and cross-section data to modeling the free-flight between collisions using a computational geometry model of the arrangements of materials. These parameters are the basis of the pdf's, which in combination with the random numbers could sample the position, energy and emission direction, information being tallied and saved further analysis [38].

3.1.1 The MCNP code

The MC code used in this project is a general purpose Monte Carlo N-Particle (MCNP) transport code developed at Los Alamos National Laboratory in New Mexico (United States)

The evolution of the computerized Monte Carlo method is said to be started in the 1940s, when scientist were working on the development of nuclear weapons in Los Alamos, even though the random sampling method have its roots much further back in history. Until the 1940s the random sampling techniques had been considered long and tedious, but during the World War II, alongside with the development of computers the random sampling methods became practical. The main use was to trace neutron movements through a fissionable material and therefore be able to solve neutron diffusion and multiplication problems in fission devices. This statistical sampling method got people to think about games of chance, where the randomness could be resolved in predictable probabilities, hence the name of the mathematical method became Monte Carlo.

Two versions of the MCNP transport code were used in this project; MCNP5, Version 1.51 [36, 39], a code which can be used to track photon-, electron- and neutron interactions and MCNPX 2.6 [37], a code in this project used to track alpha particles, but otherwise also capable of simulating other heavier particles or ions.

The MCNP can be used in several transport modes; electron only, photon only, neutron only, electron/photon and other combinations where photons or electrons are produced by different reactions. The physics of these particles and their interaction is the

basics of the MC calculations carried out by MCNP. A particle track, associated with a particle's movements trough the geometry during its whole history, is created when a particle leaves the source as well as when a new particle is created in an interaction between the first particle and the medium. The particle track for the full history depends on the cross-sections for different interactions, associated with the particle type, energy and the medium it is traversing.

3.1.2 Photon interactions

Uncharged particles, like photons, interact with matter in a way resulting in quite few interactions and a long mean-free path, since they are uncharged there is no steadily energy loss via coulomb interactions with atomic electrons. A photon interaction with matter will lead to a partial or total energy transfer of the photonic energy to the electrons of the matter, leading to a disappearance of the photon or a scatter in a significant angle with an associated energy loss.

Photons interact with matter in four different ways, each way with an associated cross-section depending on the photon energy and the material it crosses. The four interaction possibilities are; photoelectric effect (τ), coherent scattering (σ_{coh}), incoherent scatter (Compton scatter) $(\sigma_{compton})$ and pair production (κ). The total linear attenuation coefficient is given by the sum of the four cross-sections:

$$\mu = (\tau) + (\sigma_{coh}) + (\sigma_{compton}) + (\kappa) \qquad \text{Eq. 3.1.2.1}$$

The detailed physics treatment in MCNP calculations includes the coherent scattering as well as fluorescent photons occurring after photoelectric full absorption. For the coherent scattering, scattering without any energy loss, only the scattering angle is calculated, since no electrons will be produced in the interaction.

For Compton scattering, an inelastic scattering resulting in a deflection, with a specific angle, of the incident photon against an orbital electron receiving momentum and kinetic energy, the scattering angle of the photon, the new energy of the photon and hence the recoil energy of the electron needs to be determined. The energy distribution between the deflected photon and the recoiled electron is calculated using the Klein-Nishina differential cross-section formulation of the Compton angles.

Full absorption of the incident photon is explained by the photoelectric effect, resulting in the emission of fluorescent photons and/or the emission of an Auger electron. Using a photon/electron transport mode, the created particles are stored, enabling the creation of particle tracks of the emitted particles, followed by further tracking created particles.

3.1.3 Electron interactions

The interaction properties of charged particles, compared to the interaction of neutrons and photons, results in a large number of low energy loss interactions, making the simulation of electrons much more complex and time consuming. The dominating interaction is inelastic scatter against atomic electrons, resulting in a low energy loss and a small angular deflection. For the calculation of transport of charged particles, a lot of analytical and semi-analytical methods have been developed, including the use of cross section and the statistical nature of the particles for the prediction of deflection angle and energy loss.

The electron particle track needs to be deviated into many small to be able to tally a significant energy loss. The step introduced needs to fulfill the requirements of a low energy loss per step, but for at the same time a large number of collisions. A data card optional for the material cards (see section 3.2.3) is the electron substep (ESTEP) parameter. By entering ESTEP equals to an arbitrary number n, the number of electron substeps per energy step will be defined as the number n. The predetermined default step lengths, s_n, are chosen in order for the average energy loss per step is 8,3%.

$$\frac{E_n}{E_{n-1}} = 2^{-1/8} \approx 91{,}7\% \qquad \text{Eq. 3.1.3.1}$$

Applying the ESTEP card equal to a number larger than the default value for the specific material, it will subdivide these predefined steps length, s_n, by the number n; s_n/n, and thus increases the accuracy in the electron trajectory. For geometries large in comparison with s_n, the default step length probably need not to be changes, but for geometries small in comparison to s_n, the number of substeps will be crucial for the accuracy of the electron trajectory. It is recommended that all electrons in a cell undergoes at least 10 steps, substeps or not, before leaving the cell [34].

In MCNP5 1.40 a new method for the electron transport was introduced, a method not relying on pre-defined energy losses, but instead simulates the transport parameters after each electron substep taken [36]. The advantage of this new logic is mainly the more precise calculation for small cells, thus it is also more time consuming [34]. The new logic is, in the input file, introduced by the card DBCN 17J 2.

3.2 Creating a model

For MCNP to be able to simulate particle transport through a region of interest, this region has to be user specified in an input file that will be read by the MCNP, a file containing information about the [36]:

- Geometry specification
- Description of materials in the different defined structures
- Location and characteristics of the source (particles or nuclides)
- Results desired to be scored (tallied)
- Variance reduction method used to improve the efficiency
- Selection of cross-sections
- Radionuclide data

In the sub chapters following below, the different components of the input file will be discussed in more detail.

3.2.1 Geometry

When creating a model in MCNP, the user-specified geometry, becoming the design of the model, will be based on a three-dimensional configuration of cells. Surfaces are defined by the designation of the coefficients to analytical surface equations; such as planes, spheres and cylinders. In some special cases, the surfaces can be defined by defining some known

points on the desired surface, or by stating some distances between specific points on a geometrical surface.

Cells are defined as either the inside of a closed surface (inside a sphere), the gap between two closed surfaces (the frame outside a small sphere and inside a larger sphere) or outside the surface. By other means; cells are defined by or by the intersection, union or complement of regions bounded by surfaces, see picture figure 3.1 below.

Figure 3.1. The cells could be defined as union, intersection or complement of regions bounded by surfaces.. For this the schematic illustration, circles in two-dimensional space are used as a simple example.

The definition of a cell is that all points within a cell is having the same *sense* with respect to a bounding surface, which implies that all point within a cell must remain on just one side of the bounding surface. A cell defined inside the bounding surface of a sphere does only contain point with a negative sense with respect to the surface. The complement to the bounding surface, the points outside the sphere, has a positive sense with respect to the bounding surface. All surfaces therefore divide the space into two sections, one with positive, and one with negative sense with respect to the surface.

In a more general approach, the equation of a bounding surface is suggested to be: $s = f(x, y, z) = 0$. Any set of points; (x, y, z), for which $s = 0$, are points on the defined surface. For any set of points (x, y, z) for which $s < 0$ are points having a negative sense with respect to the bounding surface, and reverse, for any set of points (x, y, z) for which $s > 0$ are point with a positive sense with respect to the surface.

In the input file the cells are defined on the cell card, where each cell is described by a user-specified serial number and connected with the appropriate sense to the surface defined at the surface card. Also associated with every cell is a material number, liked to the materials listed at the material card, and a material density, see figure 3.2 below.

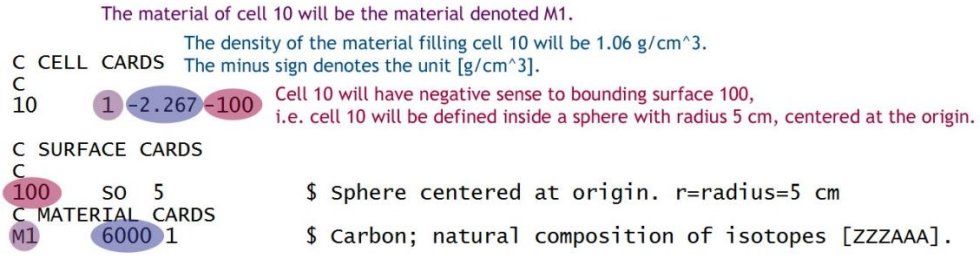

Figure 3.2. Parts of an input file, showing an example of the definition of a cell. The cell with serial number 10 has negative sense to bounding surface 100; a sphere with radius 5 cm centered at the origin of the Cartesian coordinate system. Cell number 10 is consisting of the material defined by M1 at the material card, and will have the density 1.06 g/cm^3. The minus sign ahead denotes the unit of density as [g/cm^3]. The big C used at the beginning of some rows is used for commenting.

3.2.2 Repeated structure geometry

Cells and surface boundaries which appears more than once in a geometry, the concept of repeated structures then can make it possible to replicate the already defined structure at another location in the same geometry. The concept of repeated structures will make the amount of both cell and surface definitions in the input file a lot less and therefore minimizing the time consumed while creating it, as well as and the amount of computer memory needed for a specific problem will be reduced [39].

The structure repeated could be a cell or a collection of cells requiring, as well as a cell, a boundary surface enclosing it. Optional for the user is to create a universe (u), acting as the filling material for the repeated structure. A universe could contain either a cell, a collection of cells or be a lattice, as long as the cells desired to be repeated. A lattice is an array of hexahedra or hexagonal prisms containing only one cell or a combination of cells.

The specific kind of lattice needed for the problem is defined by the lattice card LAT. LAT=1 produces a lattice made out of hexahedrons with six faces, whereas LAT=2 will produce a lattice of hexagonal prisms with eight surfaces, see figure 3.3 below. The specific lattice elements are denoted by a lattice index, [X,Y,Z], with increasing or decreasing values along the different axis, see figure 3.3 below.

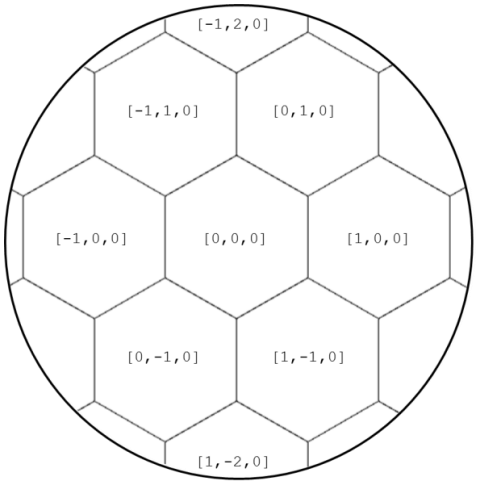

Figure 3.3. Example of a hexagonal lattice (LAT=2); each element having eight faces, enclosed in a spherical cell. The first lattice element is having lattice index [0,0,0] and the first and second indices will increase along adjacent surfaces and the third index will increase in one or the other direction along the length of the prism, giving each element an individual index.

The universe is identified by the U card, which in the input file is placed behind the sense- and surface definition in the cell card, see figure 3.4 below. The arbitrary number of the universe is user-specified and denotes what universe a specific cell is belonging to. Thus, lack of a U card or a U card with a zero entry behind the cell definition, implies that the cell is not belonging to any universe.

A cell in a universe can be filled by another universe, then introducing another level in the model. A maximum of ten levels can be used in a geometry and the hierarchy of levels will be in the opposite order to the associated number, making level zero the highest.

To fill a specified region with a universe, the FILL card is used. A non-zero entry on a FILL card indicates that the specified region (a cell) is filled with the universe with the arbitrary number equal to the non-zero entry on the FILL card, *i.e.* the cell will be filled by all the cells having the corresponding integer entry on the U card, see figure 3.4 below.

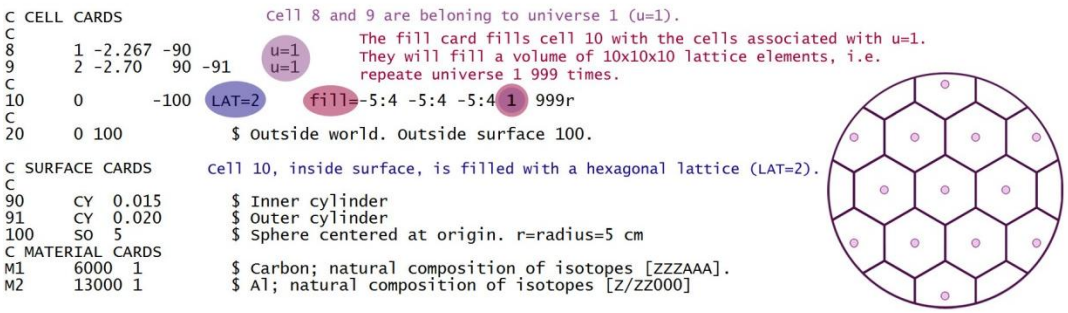

Figure 3.4. Parts of an input file, showing an example of the universe, lattice and fill concepts. Cell 8 and cell 9, defined in the cell card is associated with universe one by u=1. Cell 10, divided into a lattice of hexagonal kind by LAT=2, is filled with the cells included in universe 1. They are repeated 999 times inside the volume of cell 10, in a pattern of 10x10x10, in the x-, y- and z-direction.

3.2.3 Material and densities

The material specification is done in the material card, Mn, specifying the isotopic composition of the materials of each defined cell, thus defining what cross-sections that will be used, se section 3.3 for further information. In the Mn material card the user will have to enter an element or nuclide specific identifier on the form of ZZZAAA, where ZZZ is the atomic number and AAA the atomic mass number. Zeros on the AAA position indicates the natural composition of the element [36].

A defined material can therefore be either the natural composition of an element, or it could be a specific isotope of interest. The fraction of each element can also be specified in the material card, making it possible for a single material card, Mn, to represent *i.e.* a biological tissue or an alloy, see figure 3.5.

The specific composition of a biological tissue can be found through the National Institute of Standards and Technology (NIST) website for stopping power and range-tables for electrons, protons and alpha particles [40], based on ICRP Publication 89 [26], making it possible to simulate a wide range of common materials.

The specific densities of biological materials chosen for a specific material card, Mn, can almost certainly be found in ICPR Publication 110 [27], "*Realistic reference phantoms: an ICRP/ICRU joint effort - A report of adult reference computational phantoms*", listing the densities for materials used in the reference phantoms.

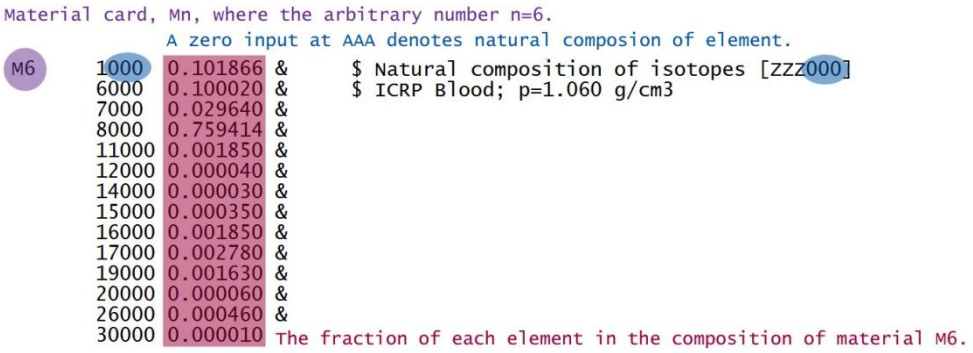

Figure 3.5. Parts of an input file, showing an example of the definition a specific material, M6, in the material card, Mn.

3.2.4 Source specification

For a Monte Carlo calculation to be carried out, the geometry defined will need to be supplemented with a source specification; containing for instance a definition of source particle type and a definition of source position and distribution. These parameters are defined on the source definition card, SDEF, describing the properties of a general source.

A source defying parameter can either be an explicit value (*e.g.* a single energy) or a probability distribution (*e.g.* a probability distribution of energies) denoted by a distribution number (Dn), needing the *Source Information* (SIn) card and the *Source Probability* (SPn) card to be defined. Source information (SIn) could, for a nuclide acting as source, be the different emitted energies possible for one particle type, and the source probability (SPn) will be the corresponding probability for each emission to occur. The Dn is connected to the specific SIn and SPn by the arbitrary number n. For the source to be described, a combination of parameters of both kinds often is used.

Some useful source definition parameters used in the general sourced definition card (SDEF) is [39]:

- PAR: Explicit parameter describing the kind of particle emitted by the source (e (electrons), p (photons) or n (neutrons)).
- ERG: Energy in MeV for emitted particles. Often a probability distribution described by the SIn and SPn cards.
- AXS: Reference vector in any direction, for EXT and RAD (see below).
- EXT: The extension of the source; defined as the distance from POS (see below) along AXS (see above).
- RAD: The radial distance of source definition from POS (see below) or AXS (see above).
- POS: Reference point for position sampling.
- X: X-coordinate of position. May define a larger region around the CEL (see below), in which source position sampling will take place.
- Y: Y-coordinate of position. May define a larger region around the CEL (see below), in which source position sampling will take place.
- Z: Z-coordinate of position. May define a larger region around the CEL (see below), in which source position sampling will take place.
- CEL: Define the specific cell or cells in which the source would be defined.
- EFF: An explicit parameter indicating the rejection efficiency criterion for the position sampling. The efficiency of rejection sampling is proportional to $(volume\ source\ region)/(total\ volume)$, since the source position will be accepted if found inside a defined source region (defined *e.g.* by a cell by the CEL card), otherwise it will be rejected. If a source region is small comparable to the region of source position sampling (defined *e.g.* by X-, Y- and Z-coordinates), the rejection efficiency criterion may need to be user-changed, to accept a larger amount of samples [38].

Figure 3.6 shows to examples of SDEF-cards, both containing explicit parameters, as well as parameters described by a probability distribution, denoted by a distribution number.

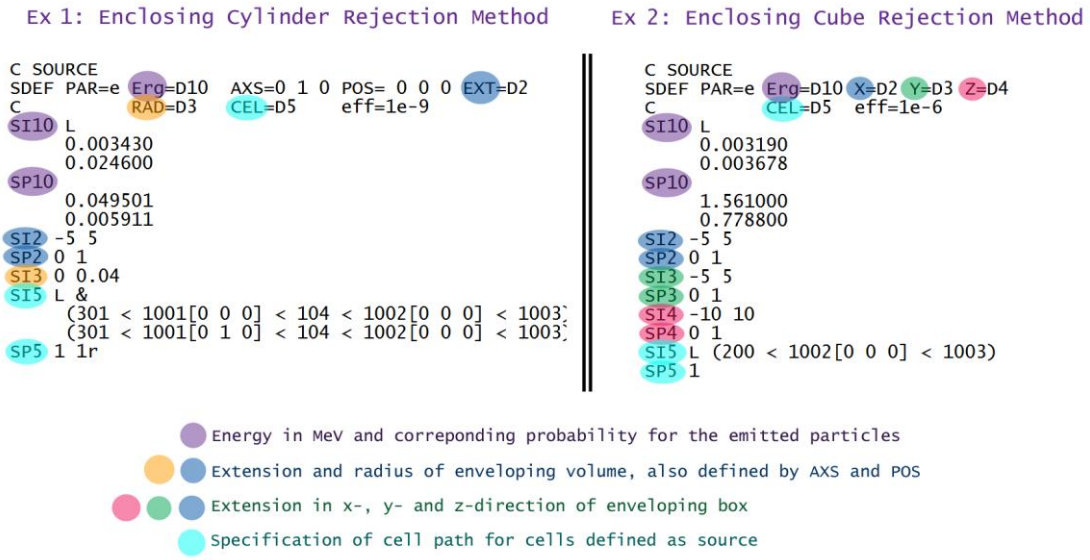

Figure 3.6. Parts of an input file, showing an example of two different SDEF-cards, one enclosing cylinder rejection method, where the cell to be source is enveloped in a cylindrical volume used for source sampling and the other example showing the enclosing cube rejection method where the enveloping volume around the cell the be source is a box defined by x-, y- and z-coordinates. A more comprehensive explanation of the parameters used for source definition is to be found in paragraph 3.2.4 above.

Using SDEF for a geometry containing repeated structures will require a different specification concerning the CEL parameter, since CEL now requires a value equal to a path of cells enclosed in parenthesis [39]:

$$(c_n < c_{n-1} < \ldots < c_0) \qquad \text{Eq. 3.2.4.1}$$

The term c_i is a cell in the universe that fills cell c_{i-1}, and if c_n is one specific element in a lattice, it is indicated with the lattice index in brackets as below:

$$\ldots < c_i\,[j1\;j2\;j3] < \ldots \qquad \text{Eq. 3.2.4.2}$$

The CEL parameter therefore will be a combination of eq 3.2.4.1 and eq 3.2.4.2 for the definition of a specific source cell in a more complex geometry with repeated structures.

3.2.5 Tallies

Tallies are used to specify what kind of information to be scored for the Monte Carlo calculation, *e.g.* flux through a surface or energy of pulses created in a detector. To score this information the user will need to specify what tally card to be used, thereby requesting the information of interest.

MCNP provides seven basic tallies, which are identified by tally type and particle type, denoted $Fn = [F1{:}F8]$. Adding an asterisk in front the tally denotation (*Fn) will change each tally into an energy tally, by multiplying each tally unit by the energy, see table 3.1 below.

Table 3.1. Listing the basic tallies provided by MCNP5 [36, 37].
<p> indicates tally available for all particles (electrons (E), photons (P) and neutrons (N)).
The # sign in the table below implies "particles".

De-notation	Description	Fn unit	*Fn unit
F1:<p>	Surface current	MeV	MeV
F2:<p>	Flux averaged over a surface	#/cm^2	MeV/cm^2
F4:<p>	Flux averaged over a cell	#/cm^2	MeV/cm^2
FMESH4:<p>	Track-length tally over a 3D mesh[◊]	#/cm^2	MeV/cm^2
F5a:N	Flux at a point or ring detector	#/cm^2	MeV/cm^2
F5a:P			
F6:<p>	Energy deposition averaged over a cell	MeV/g	Jerks/g
F7:N	Fission energy deposition averaged over a cell	MeV/g	Jerks/g
F8:<p>	Energy distribution of pulses created in a detector.	Pulses	MeV
+F8:<p>	Charge deposition	Charge	N/A

[◊] In addition to these basic tallies, MCNP also provides mesh tallies; allowing particles to be tallied on a mesh independent of the problem geometry. Implemented mesh tallies in the MCNP5 so far is only the track-length tally (F4).

3.2.7 Output

The output file does not only contain the tally information, but also additional summary information listed in tables to give the user a better understanding of the performed Monte Carlo simulation. This information could for instance concern possible errors in the geometry, the statistical relative errors corresponding to one standard deviation following a tally and the starting position and direction for a number of created source particles. This and other optional information will be printed in a number of print tables, denoted with a specific number, making them possible to either include or exclude.

Print card 10, contain information of the source coefficient and distribution will contain a parameter denoted *order*, which will hold information of the order of sampling source variables (see section 3.2.4), *e.g.* cel sur pos vec dir erg tme, information useful when creating the SDEF card for a specific source definition.

3.2.8 Methods for variance reduction

Variance-reducing techniques in Monte Carlo calculations [36] can be used to improve the precision of a given tally for a given amount of computer time.

Truncation methods are the simplest techniques for variance reduction, where parts of the phase space are truncated, eliminating part that do not significantly contribute to the estimated answer of the problem. In MCNP the specific truncation methods *energy cutoff* and *time cutoff* are available.

The *energy cutoff* in MCNP is used to terminate particles reaching an energy level lower than the cutoff energy; meaning they are regarded unimportant for further follow up and their history is terminated, a termination resulting in more possible runs in the same amount of time. The *time cutoff* in MCNP is used to terminate particles exceeding the time cutoff, therefore decreasing the computer time per history. The time cutoff should only be used in time-dependent problems, where the last time bin will be earlier than the cutoff.

Population control methods are methods artificially increasing or decreasing the number of particles in spatial or energy regions that are important or unimportant for the tally to score. In MCNP some special population control methods are used; geometry splitting with Russian roulette, energy splitting/roulette, time splitting/roulette, weight cutoff and weight windows. Widely used is the geometry splitting with Russian roulette.

The basic of the geometry splitting with Russian roulette is that the geometry is divided into important and unimportant regions; assigning importances to each cell in the problem. Particles entering an important cell are increased in number by a number proportional to the importance of the specific cell, providing a better sampling in that region. Splitting a particle into n multiple particles will assign each particle a weight inversely proportional to the multiplying number n ($weight' = weight/n$). The scored result in the tally must therefore be multiplied by the specific weight of each particle. On the other hand, particles entering an unimportant region and/or having an unimportant direction will be terminated in order not to waste computer time.

Russian roulette will be played for particles leaving a cell with an importance (I) higher than the importance (I') of the cell they are about to enter; giving ($I'/I < 1$). The probability of a particle being killed in the Russian roulette is ($1 - (I'/I)$) and thus the probability for survival is (I'/I), followed further by a weight $W \cdot (I'/I)$.

3.2.9 Estimation of errors

The result of the Monte Carlo calculation is an average of the contributions from many histories sampled during the run time of the problem; therefore the statistical error associated with each result is an important quantity.

Together with the output value for the chosen tally there also is another value presented, a value representing the estimated relative error, defined as one estimated standard deviation of the mean ($S_{\bar{x}}$) divided by the estimated mean ($\bar{x}$). The estimated relative error will be calculated after each completed MC history and will proportional to $1/\sqrt{N}$, where N is the number of histories. The value of the estimated error should be less than 0,10 for the estimated value to be considered reliable. One should be aware of that this estimation of error only refers to the precision of the MC calculation and not to the accuracy of the results in comparison to the real physical value. The accuracy of the result compared to the real value is also depending on the physical data used, the sampling techniques and the approximations done when creating both the model and the geometry. For a statement regarding the accuracy, all these above parameters will have to be taken into account [36].

Ten statistical checks are made after each tally used, including quantities *e.g.* the behavior of the estimated mean as a function of the number of histories (N), the $1/\sqrt{N}$-behavior of the estimated relative error for the last half of the problem and the decrease of the variance of the variance as a function of N for the last half of the problem. A check is answered by yes or no; a yes required for passing the specific check. Passing all checks is an assurance for the estimated answer to be found in any confidence interval created for each tally bin.

3.3 Cross-section data

Possible to include in the MCNP-code package are cross-section tables for the different kind of photon interactions, *i.e.* coherent, incoherent, photoelectric effect and pair production. The cross-section data is contained from the ENDF/B-VI8 library (the data concerning photoatomic and atomic relaxation is obtained from the EPDL97 library) and include cross-sections for nuclides with atomic numbers between 1 and 100 and for energies between 1 keV and 100 GeV [36].

3.4 Radionuclides

Decay data for the radionuclides used in this study were obtained from the Radiation Decay 3 software (Charles Hacker, Griffith University, Gold Cost, Australia). The radionuclide data was compiled by the Radiation Shielding Information Center at Oak Ridge National Laboratories, TN, USA. Data for the β-particles energy spectrum were collected from the Lund/LBNL Nuclear Data Search website [41], data originally from Evaluated Nuclear Structure File (ENSDF), updated and maintained by the National Nuclear Data Center (NNDC) at Brookhaven National Laboratory (BNL).

For the simulations carried out using the created small-scale dosimetry model for the locally absorbed dose calculations some common radionuclides were used. Both radionuclides used in diagnostics and nuclides used for therapy were chosen for the investigation, since there are of interest to compare the locally absorbed dose from commonly used radionuclides, regardless of their clinical purpose.

The nuclides used and their predominant emission is presented in table 3.2 below.

Table 3.2. Predominant emission from common radionuclides used in this study.

Nuclide	Half-life [42]	Decay type	Energy (Mean/Max)	Yield
^{211}At*	7.214 h	α α* γ	5.87 MeV 7.45 MeV 79 keV	41.7% 98.9% 21.3%
^{18}F	109.77 m	e^+	250 keV/634 keV	96.7%
^{125}I	59.408 d	e^- e^- γ	3.2 keV 3.7 keV 27.4 keV	156% 77.9% 73.2%
^{131}I	8.0207 d	β^- β^- γ	192 keV/606 keV 96.6 keV/334keV 364 keV	89.3% 7.3% 81.2%
^{111}In	2.8047 d	e^- e^- e^- γ γ	2.72 keV 145 keV 219 keV 171 keV 245 keV	100% 8.4% 5.0% 90% 94%
^{177}Lu	6.68 d	β^- β^- β^- γ γ	149 keV/497 keV 111 keV/384 keV 47.3 keV/176 keV 208 keV 113 keV	78.7% 4.7% 12.3% 11% 6.4%
^{99}Tc^m	6.01 h	e^- e^- γ γ	1.6 keV 119 keV 140 keV 18 keV	74.5% 8.8% 89% 4%
^{90}Y	64.00 h	β^-	935 keV/2.284MeV	100%

* The daughter in 58%, ^{211}Po, is included in the decay because of its short half-life of 0.52s

4 Results

The results from this project will mainly be divided into two parts; the first describing the model created and the second part describing the results obtained when absorbed dose calculations were performed with the, in the model, defined structures arranged in different source-target combinations.

4.1 The model

The small-scale dosimetry model created is based on the concept on the hepatic lobule, describing the normal cells and the normal cell architecture, descried in the theory chapter above. The specific features making the hepatic lobule significant was pinpointed, as well as structures with importance to radionuclide therapy implications. Important to be aware of when observing the design of a model or the results of the calculations is that the model is a simplification of the sketches drawn of the liver parenchyma, which in turn is a simplification of the, in some way structures chaos building the structure of the tissue. But with support from literature concerning distribution, accumulation and cell structures acting as targets, this small-scale dosimetry model may provide some understanding of the heterogeneous absorbed dose distribution origination from the heterogeneous activity distribution.

4.1.1 Microstructures in the model

Based on the concept of the hepatic lobule a small-scale dosimetry model was created. The dimensions of the microstructures use in the model were presented in table 2.7 above. The definition of each cell and structure can be seen in table 2.2. The structures mentioned in table 4.1 will all be present within the hepatic lobule. These structures will only be defined as cells at one position within the coordinate system of the lobule, since the concept of repeated structures will be used on two levels in the model; first to create the content of each lobule and secondly to create the content of the whole liver, a content consisting of repeated lobules, see figure 4.1. The whole liver is in this project defined as a sphere with a radius of 6 cm, creating a volume of approximately 905 cm^3.

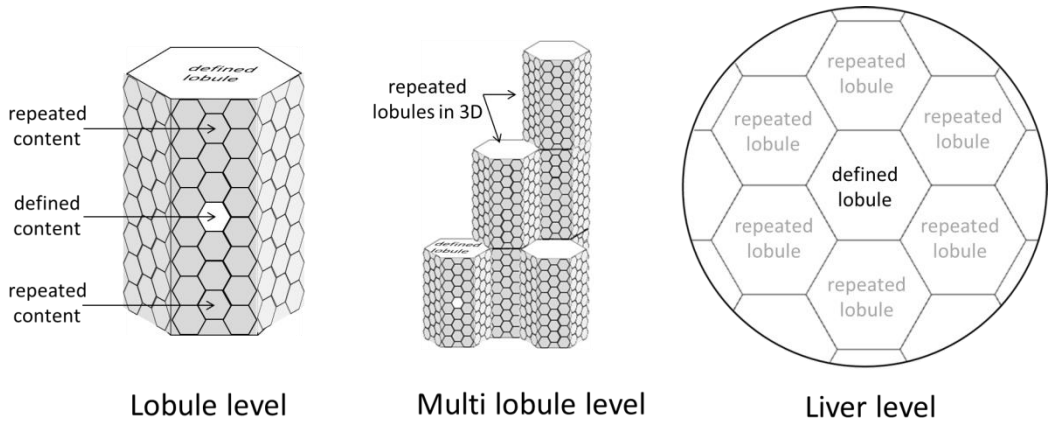

Figure 4.1. A sketch showing the two different levels of repeated structures within the small-scale dosimetry model, shown in three steps; the first creating the content of each lobule, then multiplied on top of each other and in 3 dimensions to create the content of the whole liver.

A comparison between a sketch of a hepatic lobule and the model of a lobule created can be seen in figure 4.2 and 4.3 below.

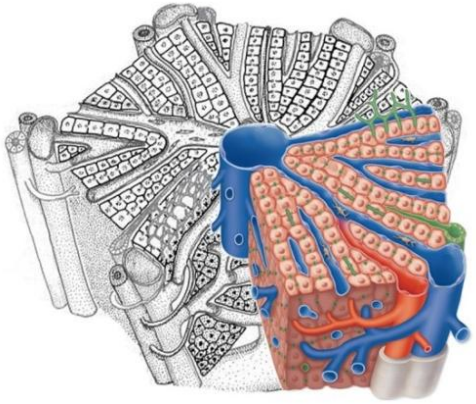

Figure 4.2. A sketch of the hepatic lobule. It is containing the most specific components of the functional unit, forming the base of the small-scale dosimetry model created. The figure is a montage, partially from [19].

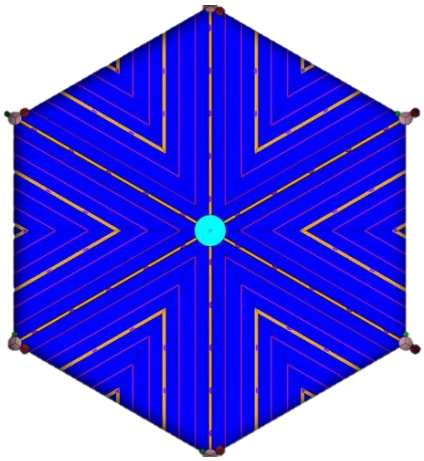

Figure 4.3. A picture showing the model of the hepatic lobule created. The model is containing the microstructures specific for the functional unit and/or important for application in nuclear medicine.

Each lobule can be divided into six wedges, centered around the central vein. A comparison between wedges of the model and the sketch of the lobule, extending from the central vein to the portal tract in the periphery of the lobule, can be seen in figure 4.4. In each of the two pictures the specific structures of the hepatic lobule is defined and a conclusion concerning the presence of the different kind of microstructures is that it is repeated many times in a specific pattern across a wedge.

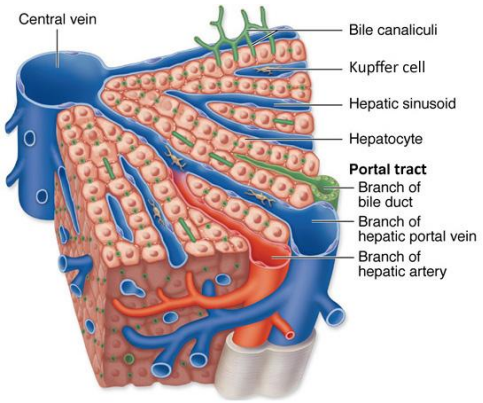

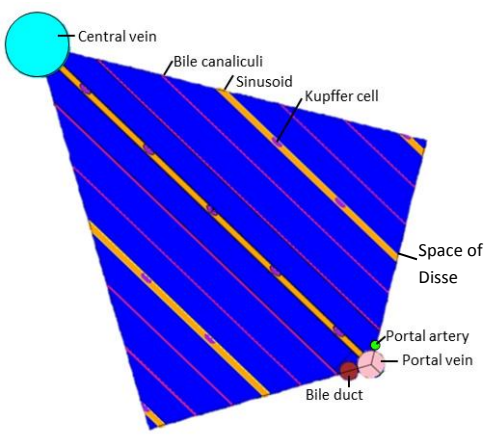

Figure 4.4

The sketch of a wedge of the hepatic lobule, acting as an inspiration for the design of the small-scale dosimetry model. Picture from [19].

A wedge of the created model, inspired by the sketch seen to the left, with the defined structures highlighted.

The content of the six wedges building one lobule is identical, but rotated 60 degrees relative each other in order to generate a lobule. Therefore each portal tract will have a sinusoidal connection with the central vein. The wedges are delimited by three surfaces criss-crossing the hexagonal prism outlining the lobule, which intersects the outer border of the lobule at the midpoint of each side of the hexagonal prism, making each wedge unique regarding the sense to two of the three delimiting surfaces. A fill card is used to fill each wedge with the cells belonging to the universe forming the filling material of each wedge, see figure 4.5. The fill card can be combined with a transformation card, defining the angle of rotation applied on the universe filling each specific wedge. Different transformations therefore are used for the six different wedges.

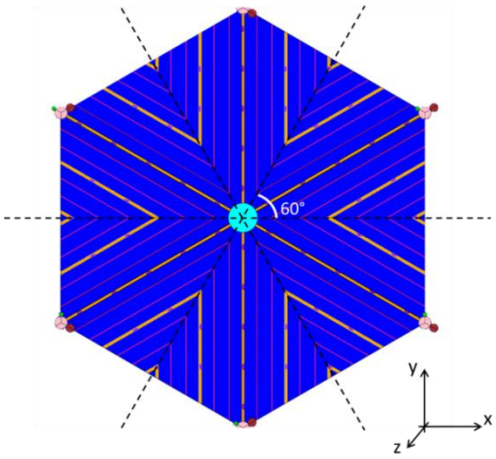

Figure 4.5. The six wedges forming one lobule are filled with the same repeated structures, only defined once, but belonging to the same universe. A fill card is used, filling the different wedges delimited by the three surfaces crisscrossing the lobule. The fill card containing to each wedge is associated with a transformation card, rotating the filling universe a desired angle.

The lobule, with the height of 2 mm is then repeated in another hexagonal lattice in three directions, creating the whole liver sphere of 905 cm^3, see figure 4.11. Due to the repetition, each lobule is placed on top of each other, thereby making the delimitation in height non important.

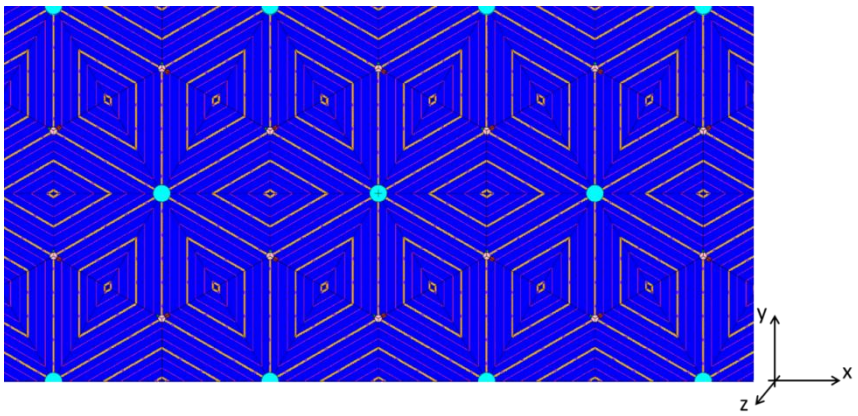

Figure 4.6. The six wedges (= one lobule) is in turn belonging to a universe, making it repeatable in another hexagonal lattice, building the volume of the whole liver.

The xz-plane perpendicular to the xy-plane shown in figure 4.5 and figure 4.6 above can in some different cross sections be seen in figure 4.7.

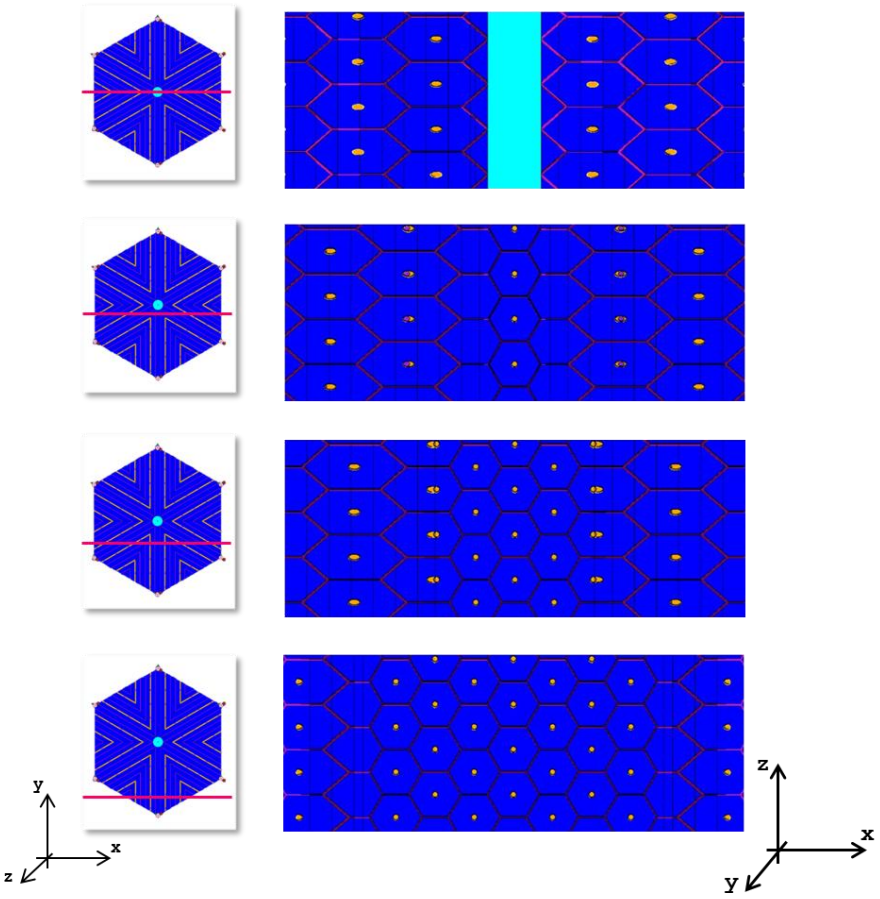

Figure 4.7. The figure shows the cellular structure of some different xz-planes in the small-scale dosimetry model, planes perpendicular to the xy-planes., shown to the left in the figure. The cross sections are shown as a function of decreasing y-position.

The content of a wedge is the hepatocytes, the sinusoids, the Kupffer cells, the bile canaliculi and the space of Disse. By the use of repeated structures each kind of structure becoming part of the content of one wedge is only needed to be specified once; *i.e.* one unit containing hepatocytes, sinusoids, Kupffer cells, bile canaliculi and space of Disse needs to be defined in the input file.

Inside a biologic lobule, each hepatocyte is in contact with both blood and bile, allowing the direction of transport through the hepatocytes to be from blood to bile. Between each hepatocyte and the closest sinusoid, the small area space of Disse is present. The design of the cells building the content of the wedge in the model therefore will be a hexagonal frame representing the bile canaliculi, enclosing the hexagonal shaped hepatocyte which will be in direct contact with the space of Disse, enclosing the sinusoid, see figure 4.8; showing the xz-plane according to the Cartesian coordinate system used in MCNP. The y-axis of figure 4.8 is orthogonal to the plane where the wedges are present.

One of these units of defined cells will belong to a universe, repeated according to the lattice prisms defined by LAT=2, resulting in a hexagonal pattern of units, all running along the axis between the central vein and the portal tract.

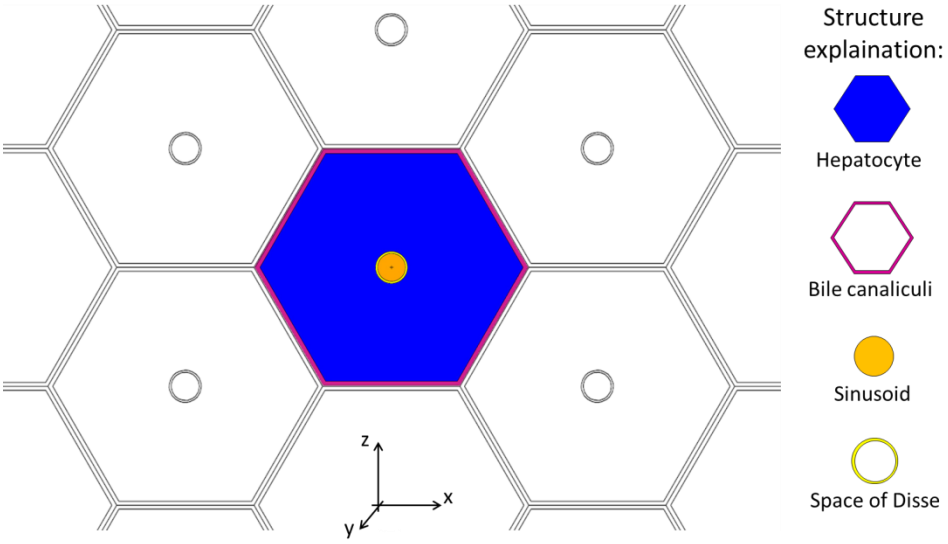

Figure 4.8. The content of the wedges, including the enclosing frame representing the bile canaliculi contains a hexagonal shaped hepatocyte plate and a cylindrical sinusoid framed by a cylindrical shaped space of Disse. These cells are the only structures defined in a wedge and the unit created, containing the defined cells, is repeated in a hexagonal lattice pattern, filling the volume of the wedge.

The dimensions of the microstructures defined in the wedge are shown in figure 4.9. The bile canaliculi, acting as a frame for each hexagonal hepatocyte plate is 1 μm. Since each unit enclosed by the frame always is adjacent to a replica of itself, the total thickness of the bile canaliculi in the model will be 2 μm thick. The distance between the blood and the bile, *i.e.* the bile canaliculi and the sinusoid, will be approximately 29 μm, a distance suitable for the size of the hepatocytes.

The microstructures in the lobule are in MCNP defined by surfaces becoming the outer border of the cells representing the different microstructures. The sinusoid is defined by a cylinder surface denoted by CY; a cylinder on the y-axis. The sinusoid cell therefore will have negative sense with respect to the CY-surface. The cell representing space of Disse also is represented by a cylinder, in the same manner as the sinusoid, but with a slightly larger diameter compared to the sinusoid. The space of Disse will thus have negative sense to the cylinder with the larger diameter and a positive sense to the smaller cylinder, defining the tubular space between the cylinders as the cell representing the space of Disse, see figure 4.9.

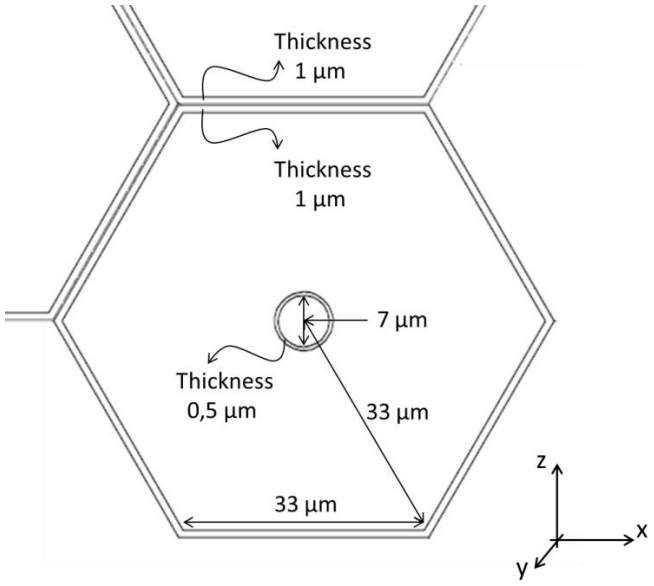

Figure 4.9. The figure shows the dimensions of the structures defined within a wedge, *i.e.* bile canaliculi, sinusoid, Space of Disse and the hepatocyte.

The hexagonal cells representing the hepatocyte and the bile canaliculi are defined by six planes rotated 60 degrees relative to each other, with the extent equal to the height of the lobule. The planes used were general planes (P) and planes normal to the z-axis (PZ). As for the cylinders, two border surfaces were created, one inner and one outer. The hepatocyte, defined inside the inner surface border, will have negative sense to the three upper planes and thus positive sense to the three lower planes; see the left part of figure 4.10 below.

The bile canaliculi will like the space of Disse be defined as the frame between the outer surface border and the inner surfaces. Concerning the sense relative the defined planes, the bile canaliculi will have negative sense to the outer three upper planes and positive sense to the outer three lower planes. Concerning the, with respect to the bile canaliculi, inner planes the planes needs to be in a union to be able to create a border surface for the cell containing the bile canaliculi. The union operator in MCNP is allowing concave corners, useful for the creation of the bile canaliculi.

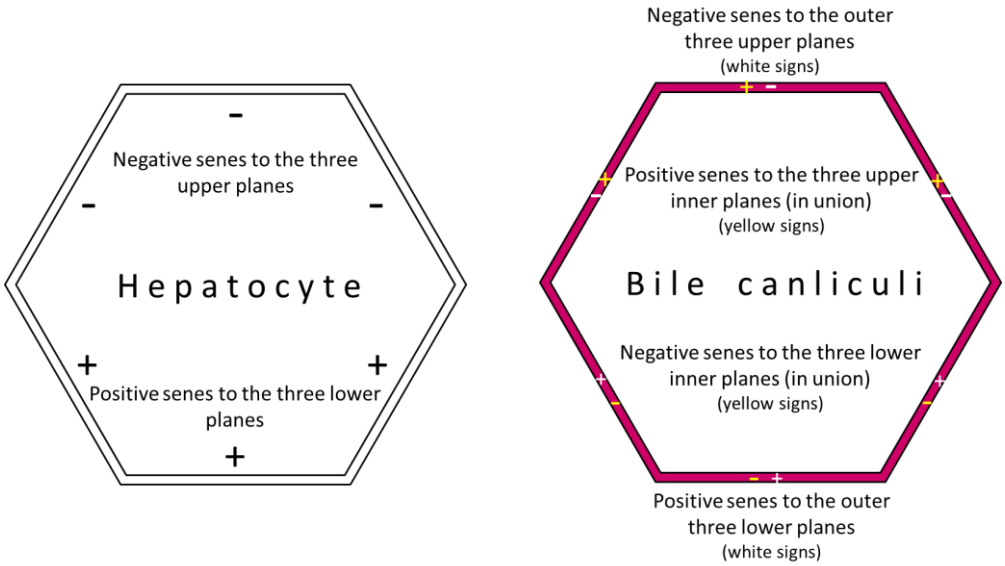

Figure 4.10. The figure is illustrating the sense of each cell, with respect to the different bounding surfaces, consisting of different planes, rotated 60 degrees with respect to each other. The sense to the planes delimiting the hepatocyte is seen to the left and the sense to the combination of planes delimiting the bile canaliculi is seen to the right.

The hexagonal prism cell forming the hepatocytes and the Space of Disse will, along the y-axis, be divided into slices, delimited by equidistant surfaces, perpendicular to *e.g.* sinusoids. The thickness of the hepatocyte slices is user defined, but a reasonable distance between the surfaces should be about the size of the hepatocytes, 20-40 μm [9, 19]. In figure 4.11 below, the thickness of the hepatocytes is 25 μm. The division of the hexagonal prism and the Space of Disse into slices also enables the creation of a line of targets along the axis from the central vein to the portal fields, in turn enables the detection of absorbed dose gradients from the central vein or portal tract. Concerning the detection of gradients, the slices of hepatocytes could be divided into even smaller structures, allowing a more detailed calculation of the absorbed dose distribution.

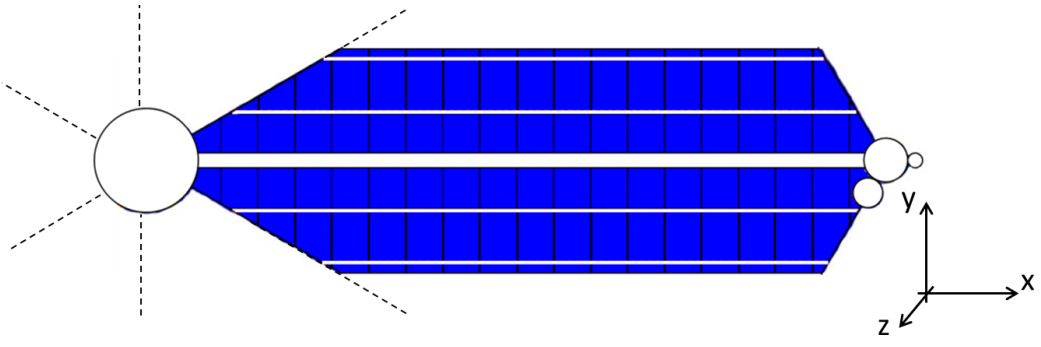

Figure 4.11. The figure shows the division of the hexagonal prism into hepatocytes with a thickness of the same magnitude as the cellular size. The cells created between the delimiting surfaces also acts as target cells in the absorbed dose simulation and calculation. In the same manner also the Space of Disse is divided in to smaller structures, enabling the detection of an absorbed dose gradient.

When dividing the larger structures into smaller, the new structures must have a cell index. The numbering is defined along the axis from CV to portal tract, an all cells at the same position along that axis will have the same cell index, thus belonging to different repetitions of the hepatocyte unit, thereby having different lattice indices, see chapter 4.1.2 below.

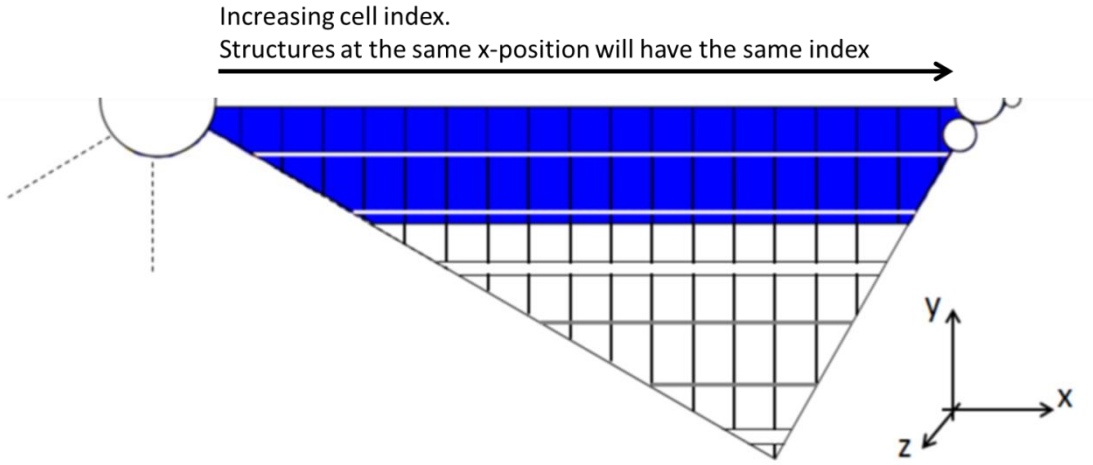

Figure 4.12. The figure shows and expansion of figure 4.8 for displaying the numbering system, giving all divisions of the hepatocyte and the Space of Disse a cell index. Structures having the same horizontal position will have the same cell number, running from *n* to *n+n*.

The liver specific macrophages, the Kupffer cells, are residing inside the sinusoids and are thus structures defined in the same universe as the other structures used for filling the wedges. The Kupffer cells in the model is delimited by ellipsoid surfaces, with the major radius length equal to 8 μm and the minor radius length equal to 3,5 μm, positioned along the sinusoidal surface, inside in sinusoidal volume.

The Kupffer cells are not evenly distributed throughout the hepatic lobule, but are more numerous in the periportal region. Since the three zones in the lobule not are strictly defined, the percentage distribution mentioned in chapter 2.1.3 is not strictly fulfilled. The distribution of the Kupffer cells in the approximated three zones of the model can be seen in figure 4.13. Two slices in the xy-plane of the model will be shown, representing the two slightly different xy-planes existing in the model. The origin of the different planes is the hexagonal pattern of the lattice elements filled with the universe containing the specific cells of the liver. The stacking pattern, with origin in the sinusoid, of these planes will between each plane be shifted 0,75 times the unit (the hexagonal hepatocyte plate framed by the bile canaliculi) in the x direction and 0,5 times the unit in the z-direction. See the upper part of figure 4.13 below.

In pair of the two existing xy-planes in the model, 120 Kupffer cells are present. The percentage distribution of the Kupffer cells in the three zones is 55% of the Kupffer cells in the periportal zone 1, 40% in zone 2 and 5% in perivenous zone 3. The percentage distribution in each zone is highly dependent on the borders delimiting the three different zones, whereas a distribution accurate enough could be a non-homogeneous distribution over the radius of the lobule, with a higher concentration of Kupffer cells in the periportal region.

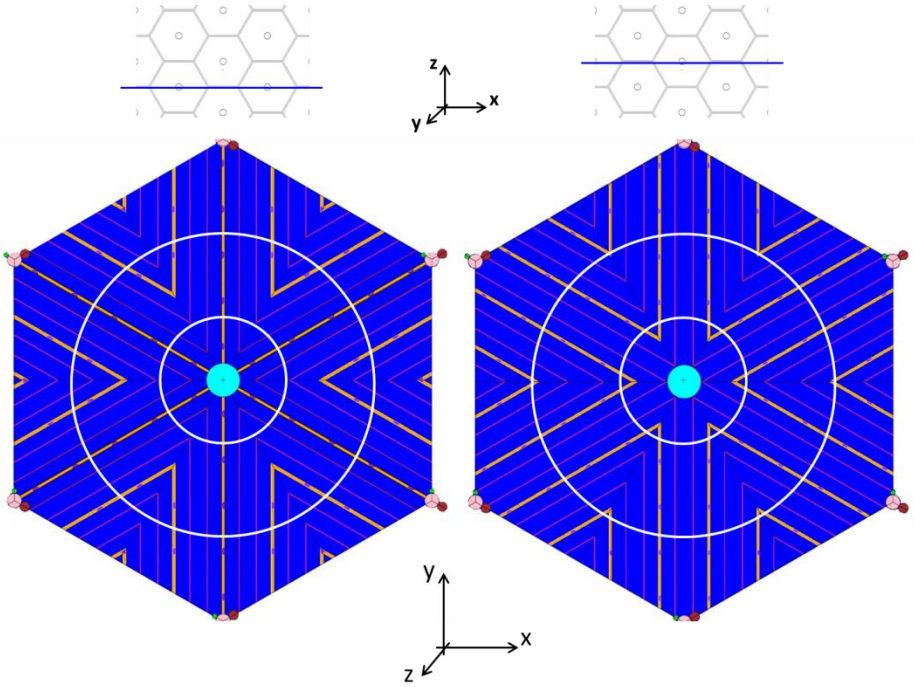

Figure 4.13. The distribution of Kupffer cells in the hepatic lobule is heterogeneous and percentage distribution in the different acinus zones of the hepatic lobule is suggested by Dancygier [21]. The figure shows an assumed division of a lobule into the three zones, an assumption made since no strict definition of the border between the zones exists.

4.1.2 Source definition within the model

All structures defined in this small-scale dosimetry model can act as source and/or target and the source definition card (SDEF) therefore has to be defined in quite different ways, depending it´s position.

If the source is placed in the central vein or in some structure in the portal tracts, an enclosing cube rejection method is used, using the parameters X, Y, Z and CEL defined in the source specification chapter 3.2.4. By defining a box of X, Y, Z, enveloping the desired source cell wherein the source samples are taken and accepted if within the defined CEL.

For the cells building the unit of the hepatocyte slice framed by the bile canaliculi to act as a source, the source definition card, SDEF, is expressed as a cylindrical source, thereby using the enclosing cylinder rejection method (also described in chapter 3.2.4). The radius of the cylinder used for source region sampling may differ depending on the cell defined on the CEL card, since differently wide cylinder will be needed for the hepatocytes acting as source, compared to if the sinusoids acts as source.

When defining a source by the number of that specific cell, all the repetitions of that cell will act as source as well. If one wishes to delimit the source to a specific lobule or a specific wedge or even one specific cell, one need to define the source with knowledge of the unique lattice index of each lattice element in the model.

Each lattice element is associated with two lattice indices, the 1st Lattice Index and the 2nd Lattice Index. These two lattice indices, defined in two different direction makes each lattice element unique and possible to refer to. The 1st Lattice Index (written in red in figure 4.14 below) is defined having the same index along the z-axis, with increasing indices along in the direction of the positive x-axis and decreasing indices along negative x-axis.

The 2nd Lattice Index (written in blue in figure 4.14 below) is defined along a diagonal line with increasing indices for increasing z-coordinates and decreasing indices for decreasing z-coordinates. Each voxel inside the lobule is indicated with a x- and a y-coordinate. The minimum, absolute, x-position will be denoted xp and the corresponding y-position will be denoted yp. For a cell to be denoted source, xp and yp exist must exist in a lattice element existing in the lobule. The absolute minimum position in x-direction, xp, will be different for *e.g.* hepatocytes and Kupffer cells. For the hepatocyte to count as source, the corner of the hexagonal prism closest to the z-axis needs to be inside the lobule border, while for the Kupffer cell to count as source, the midpoint of the hexagonal prims needs to be inside the lobule.

The expression for the xp and yp for will be sampled over $xdim$ (the maximum absolute value of existing lattice indices in x-direction) and over $ydim$ (the maximum absolute value of existing lattice indices in y-direction), see figure 4.14. If the received xp and yp for a specific lattice element exists inside the lobule, the cell is accepted as a source and printed to the CEL parameter in the CEL card.

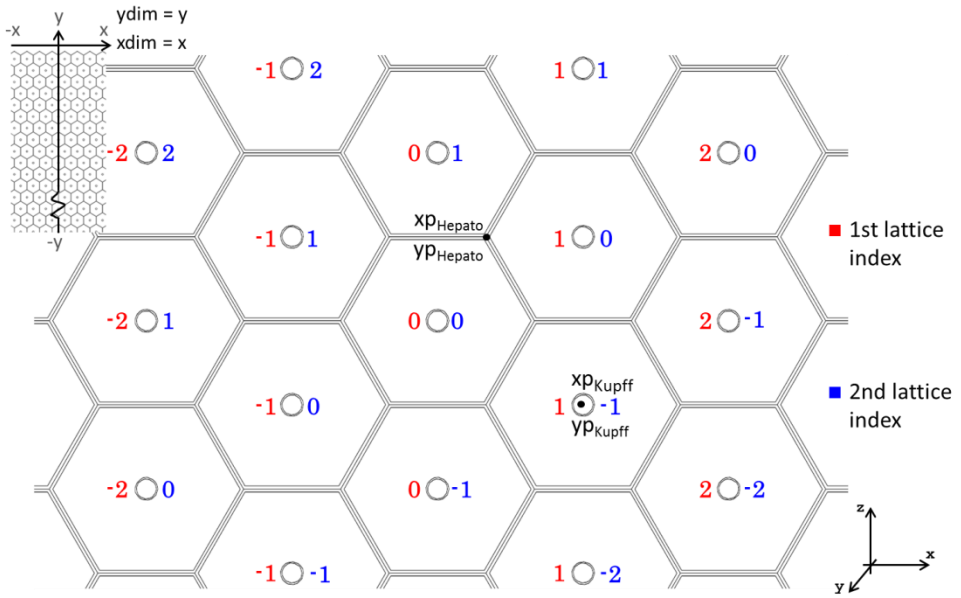

Figure 4.14. An illustrating of the two different lattice indices used for the source definition of structures. The absolute minimum position, xp and yp, for a cell is different for different cells and for different lattice elements.

4.1.3 Volume density of cells

The volume density of the different cells in the small-scale dosimetry model is of interest for a comparison with the volume density of the biological data presented and to receive the mass of each structure included in the model. A stochastic estimation of the volumes is done by using the VOID card, a card removing all the material, density and cross sections associated with the defined cells in the model. The VOID card also sets all nonzero importances to one, making it possible to run many particles in a very short time. To flood the voided volume with particles it has to be enclosed inside a planar source with the source weight equal to the surface area, *i.e.* an inward directed spherical surface with the weight equal to $4\pi r^2$. The cell flux tally (F4, see table 3.1 above) is used to score the volumes and if the unit flux (particles/cm^2) is used, the output of the tally will be the volumes of each defined cells. The source distribution is biased from the default cosine distribution using the source bias parameter, SBn, to create a higher track density towards the center of the sphere. The output thereafter gives the volume of each defined cell in the geometry. In table 4.2 below the volume density of the different structures are presented.

Table 4.2. Composition of the liver, divided into percentage of cell type and compartment for the biological distribution and the distribution obtained in the small-scale dosimetry model. A combination of table 2.6 and the data received from the stochastic volume calculation.

	Biological distribution	**Model distribution**
Cell type/compartment	**Volume density (%)**	**Volume density (%)**
Blood	30,5	2
Bile	1,4	6,7
Hepatocytes	53	90,7
Non-hepatocytes	4,2	1,2
Sinusoidal space	1,9	1,1
Kupffer cells	1,4	0,1
Stellate (Ito) cells	0,9	-
Extracellular space	10,9	0,4 (Space of Disse)

4.2 The absorbed dose calculation

The aim of this small-scale dosimetry model is to calculate the locally absorbed dose to the microstructures in the liver. These microstructures are defined in the model and their biological properties and their roll in radionuclide therapies was described in the chapters above, as well as their geometrical descriptions in the model. In this chapter some results from performed Monte Carlo calculations will be presented and the multipurpose function of the model will be demonstrated.

The small-scale dosimetry model can be used to calculate cross-doses as well as self-doses for a desired source-target combination. Since the actual target in the hepatic tissue leading to lethal radiation damages is not known [30], the flexibility of the model to choose different source-target combinations is an advantage.

The new treatment techniques introduced in the field of nuclear medicine, where very high absorbed doses are delivered, in combination with the knowledge of a non-uniform radiopharmaceutical distribution there is a need for a reassessment of the absorbed dose specification from internal emitters. The aim of the creation of this small-scale dosimetry model is to compare the conventional approach of the MIRD formalism; a calculation of the mean absorbed dose to a whole organ, to the locally absorbed dose to a defined microstructure within the small-scale dosimetry model. The results therefore will be presented as the ratio between the local absorbed dose to a defined microstructural target from accumulated activity in a microstructural source, divided by the mean absorbed dose to the whole volume of the organ originating from the accumulated activity in the same microstructural source region. According to Equation 2.2.2, the ratio between the absorbed doses can be expressed as follows:

$$\frac{D_{region}}{D_{mean}} = \frac{\tilde{A}_{region}}{\tilde{A}_{mean}} \cdot \frac{S_{region}}{S_{mean}} \qquad \text{Eq. 4.2.1}$$

Since the accumulated activity, $\tilde{A}_{region}$ and $\tilde{A}_{mean}$ in equation 4.2.1, has to originate from the same source region for this absorbed dose calculation comparison to be interesting, they will cancel out. In combination with equation 2.2.6, describing the terms in the S-factor, the resulting equation will look as follows:

$$\frac{D_{region}}{D_{mean}} = \frac{S_{region}}{S_{mean}} = \frac{\frac{\Delta \cdot \phi(r_T \leftarrow r_S)}{m_{region}}}{\frac{\sum \Delta \cdot \phi(r_T \leftarrow r_S)}{\sum m_{region}}} \qquad \text{Eq. 4.2.2}$$

Since the absorbed dose calculation comparison will be carried out for one nuclide at the time, the equation can be simplified to equation 4.2.3 below:

$$\frac{D_{region}}{D_{mean}} = \frac{\frac{\phi(r_T \leftarrow r_S)}{m_{region}}}{\frac{\sum \phi(r_T \leftarrow r_S)}{\sum m_{region}}} \qquad \text{Eq. 4.2.3}$$

Equation 4.2.3 above can, according to the MIRD formalism, be expressed as the ratio between the specific absorbed fraction and the sum of all absorbed fractions divided by the total mass of the volume. Required for this absorbed dose calculation comparison

therefore will be the absorbed fractions, $\phi(r_T \leftarrow r_S)$ and the mass of the individual regions, m_{region}. The volume of each structure is achieved by the stochastic volume calculation, described in chapter 4.1. The volume received per cell is thereafter multiplied by the density (1.00 g/cm^3 for hepatocytes, space of Disse and Kupffer cells, 1.03 g/cm^3 for bile ducts and canaliculi and 1.06 g/cm^3 for blood) associated to each cell, giving the mass of each cell.

The source activity was assumed to be uniformly distributed within the source different region, making the uniform isotropic model still hold true, thus on a microstructural level. The source will be placed in one or many structures (defined by cell number) in one (or seven, for the case of absorbed dose ratio simulations to achieve better statistics). The absorbed energy will be tallied over all cell numbers in the whole liver volume. Because of the repeated numbering of cells, the tallied energy in one cell number will represent the total absorbed energy for that cell number throughout the whole liver volume. The total mass of that structure will be the m_{region} in the MIRD-formalism, resulting in a mean absorbed dose for each specific cell number. This is manageable due to the dose reciprocity theorem, since the spill out from one lobule would represent the spill in from an adjacent lobule, provided that the escape of energy from the whole volume is negligible (see estimation in figure 4.27).

From the absorbed energy in every region, obtained by the *F8 tally; the absorbed fractions, specific absorbed fraction and S-values can be calculated, according to the MIRD formalism. Some results presented in this master thesis will be based on the dose ratio between the locally absorbed dose and the mean absorbed dose, described by eq. 4.2.3 above, applicable to both self-doses and cross-doses.

The simulation of different particle type, although resulting from the same radionuclide, is simulated separately and independent of each other, *i.e. e.g.* photons, electrons, beta-particles and alpha-particles were performed separately, resulting in one output file per emitted radiation type. Since MCNP5 only allows simulation of photons, electrons, positrons and neutrons, MCNPX 2.6 was used for the simulation of alpha-particles from *e.g.* ^{211}At, but was restricted to only nuclides emitting alpha-particles, since MCNPX 2.6 does not contain the new energy logic for electrons, described in short terms in section 3.1.3.

The absorbed energy in each defined region will be tallied by the energy deposition tally denoted *F8, scoring the absorbed energy in MeV in each region. After all simulations, with just one MC code or at some occasions with both MCNP5 and MCNPX, the absorbed energy in one region, originating from each particle type emitted, were summed up with consideration taken for the radiation yield. The number of simulated particles for the simulations was about 10^6 in order to keep the relative errors below 1% and to pass all statistical checks performed after each history run.

As an illustration of absorbed dose distribution a mesh tally can be used to tally particles independent of problem geometry. In figure 4.15 the mesh tally FMESH4 was used to tally the electron component and/or the beta component of the nuclear transition, illustrated as the flux [particles/cm^2] for three common radionuclides, ^{125}I, ^{99}Tc^m and ^{90}Y for the source placed in all the Kupffer cells in 7 lobules.

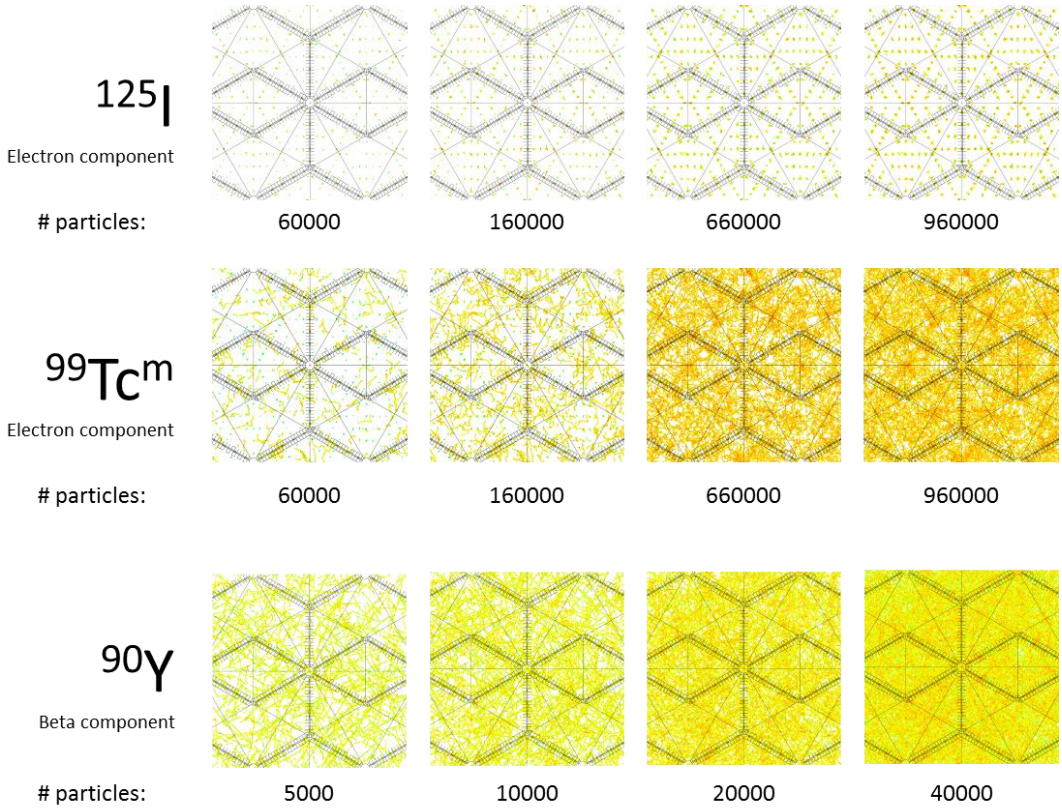

Figure 4.15. An illustration of the particle flux in particles/cm^2 for the electron and/or beta component for three nuclides. The number of particles simulated to achieve each figure is indicated below each subpart of the figure.

For some results presented in this master thesis, the target cells will be positioned along the x-axis, from the center of central vein (0 μm from center of CV) to the corner of the lobule, in the portal tract (500μm from center of CV). One hepatocyte slice will represent all slices with the same number, present in all existing lobules. Figure 4.16 shows the part of the model acting as "result visualizer".

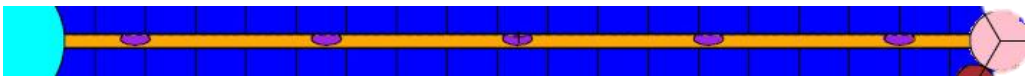

Figure 4.16. An illustration of the sliced hepatocytes which is one example of targets regions. They will be represented along the x-axis in the following graphs showing the results of the Monte Carlo simulations of the absorbed dose ratios. The Kupffer cells are denoted nX, where X runs from [0:4].

The absorbed fraction, $\phi(r_T \longleftarrow r_S)$; the fraction of energy emitted from the source region, r_S that is absorbed in the target region r_T is achieved by dividing the absorbed energy, $\Delta_i \cdot \phi_i(r_T \longleftarrow r_S)$, tallied by the *F8-tally, by the average emitted energy per decay, Δ_i. The absorbed fraction from photons is not of much interest, since the range of emitted photons greatly excess the length of the microstructure defined in the small-scale dosimetry model. The absorbed fraction of charged particles, *i.e.* electrons, alpha particles, positrons and beta particles, therefore are of more interest.

4.2.1 Absorbed fractions

The absorbed fraction from the charged particles is achieved by dividing the tallied absorbed energy from charged particles only by the averaged emitted energy per decay originating from the charged particles. By defining the source within one of the Kupffer cell positions (n3) in one lobule, the absorbed fraction in different structures could be investigated by tallying the absorbed energy in the whole volume. The absorbed fraction from charged particles in the hepatocytes could be seen in figure 4.17, in the Space of Disse in figure 4.18 and in the Kupffer cell itself in figure 4.19.

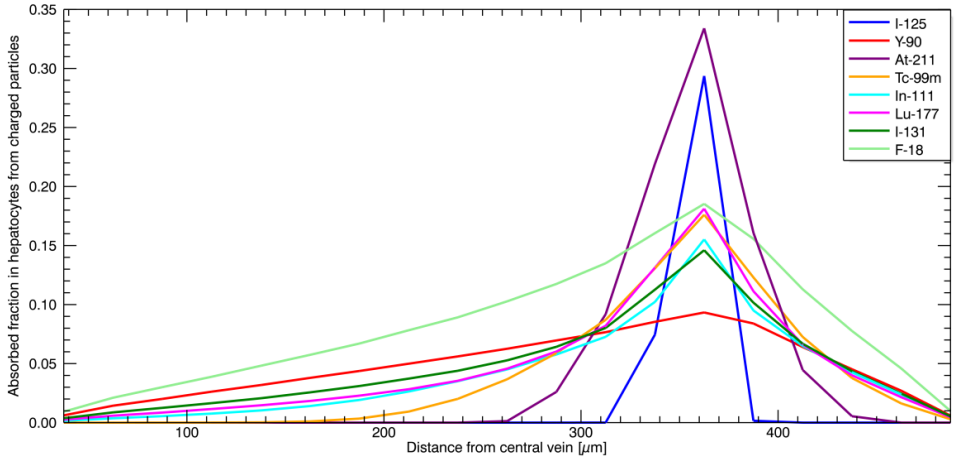

Figure 4.17. The figure shows, from eight common radionuclides, the absorbed fraction in the hepatocytes from emitted charged particles accumulated in the Kupffer cells positioned at 355µm distance from the central vein. The x-axis in the figure is representing the radius from central vein to portal tract, 37,5 µm to 487,5 µm.

The absorbed fraction from charged particles emitted from the Kupffer cells is the highest in the hepatocytes in the close vicinity of the Kupffer cell. For the two radionuclides ^{211}At and ^{125}I, the absorbed fractions will be the highest, indicating a local absorption of the emitted energy. ^{90}Y on the other hand will spread its energy across the whole lobule, thereof the wedge-like shape of the ^{90}Y-absorbed-fraction-curve in figure 4.17.

The absorbed fraction in Space of Disse is presented in figure 4.18, and will be the highest for ^{125}I.

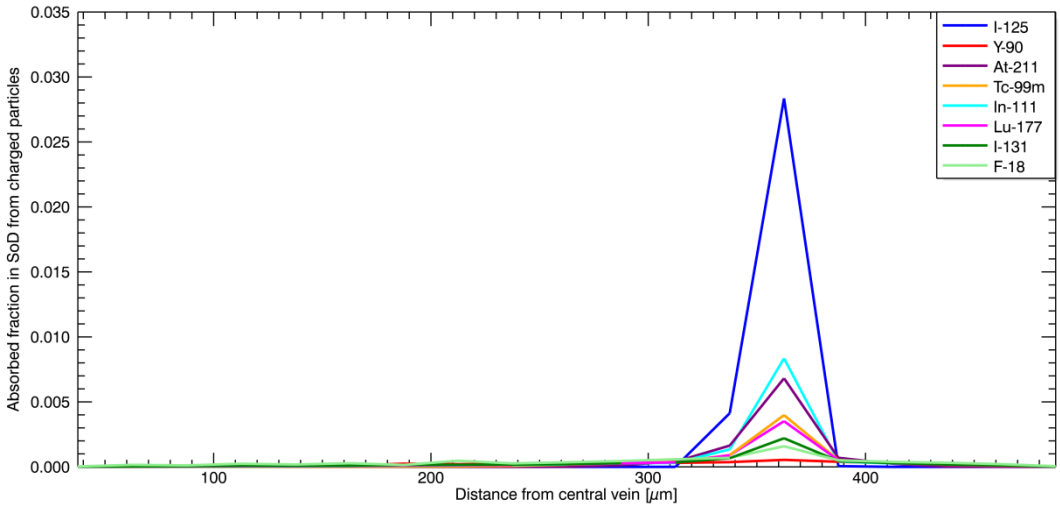

Figure 4.18. The figure shows, from eight common radionuclides, the absorbed fraction in the Space of Disse from emitted charged particles accumulated in the Kupffer cells positioned at 355µm distance from the central vein. The x-axis in the figure is representing the radius from central vein to portal tract, 37,5 µm to 487,5 µm.

The absorbed fraction from charged particles in the Kupffer cells themselves can be seen in figure 4.19. The values presented are the mean value of the absorbed fractions for all Kupffer cells exciting in the model.

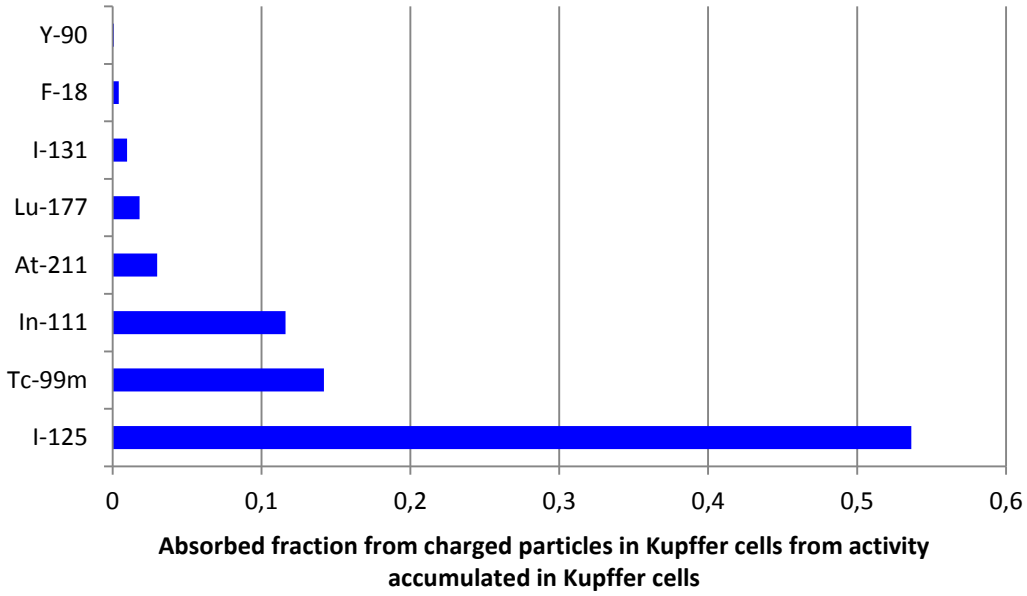

Figure 4.19. The diagram above shows the absorbed fraction from charged particles in the Kupffer cells from activity accumulated in the Kupffer cells. The different radionuclides are found on the y-axis and the absorbed fraction along the x-axis.

In figure 4.19 one can see that the self-absorbed fraction in the Kupffer cells is, as for the Space of Disse, lower for ^{211}At than for ^{125}I, in contrast to the more similar absorbed fraction in the hepatocytes, shown in figure 4.17. The energy from charged particles emitted from ^{125}I, principally low energy electrons with a range suitable for absorption within the source itself, *i.e.* the Kupffer cell, gives them a high self-absorbed fraction. In contrast, the absorbed fraction for the alpha emitting isotope ^{211}At, is assumed to be principally absorbed in the hepatocytes, since the emitted alpha particles, with an energy of 5,87 MeV will have a projected range of about 50 μm [40], and thus the Bragg peak will appear previous to the projected range. The absorbed fraction in the source itself from the radionuclide ^{90}Y will be very small, since the long range of the emitted particles will spread the absorbed energy across the whole lobule.

The absorbed fraction from activity distributed in the blood, *i.e.* the central vein, the sinusoids and the portal tract is presented in figure 4.20, more specifically; the activity in the portal field is specified to be in the portal artery, a scenario in question for the SIRT therapies.

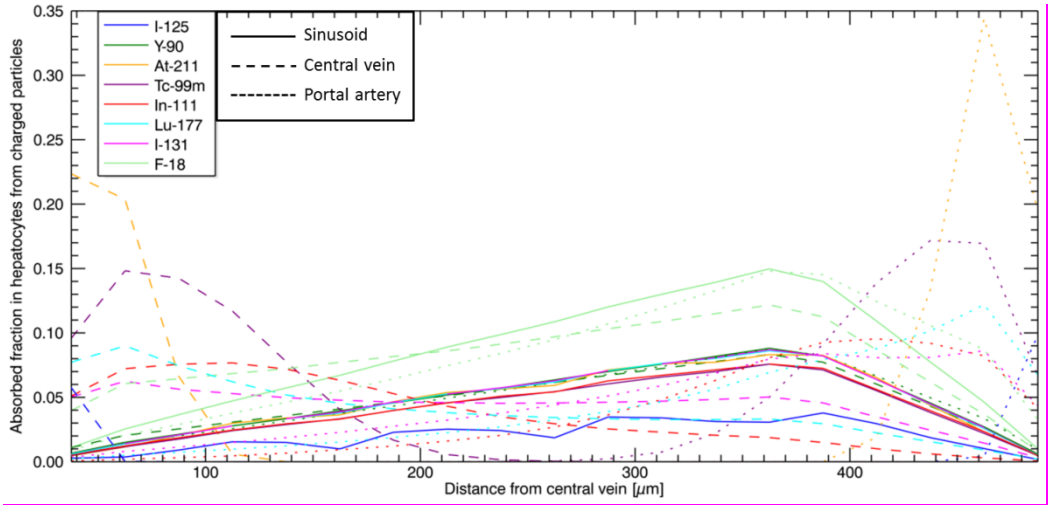

Figure 4.20. The figure above shows the absorbed fraction in the hepatocytes from activity placed in the blood, i.e. the central vein, the sinusoids and, in this example, the portal artery. The three structures are acting as individual sources in the simulation and are indicated with different line styles in the plot above.

For ^{90}Y, the radionuclide labeled to the SIRT microspheres, the absorbed fraction in the hepatocytes looks identical independent of source structure. The absorbed fraction in the hepatocytes from radionuclides in the central vein are lower than the absorbed fractions originating from activity in the portal artery, since the diameter of the portal vein is wider and a larger amount of energy will be absorbed in the source itself. For ^{125}I located in the sinusoids the presence of Kupffer cells is visible in the graph above. The dips in the curve occur where the Kupffer cells are present, acting as ellipsoids without activity. The absorbed fraction from ^{99}Tc^{m} is for activity placed in CV and portal artery quite high for the hepatocytes in their vicinity. The biological implication of that is still not known, but will certainly be connected to the half-life of the radionuclide, which for ^{99}Tc^{m} is quite short.

4.2.2 Absorbed dose ratios

As indicated in the beginning of this chapter, the ratio of the locally absorbed dose and the mean absorbed dose to the whole volume, origination from the same source will be presented for the hepatocytes, the Space of Disse and the Kupffer cells. The source is placed inside all available Kupffer cells in 7 lobules in the center of the liver volume, but targeting the absorbed energy in the whole liver volume.

Figure 4.21 shows the dose ratio for the hepatocytes. The straight black line at the ordinate value of one represents the mean dose to the whole volume. Since we are observing the cross-dose, the integral under the colored lines will not be equal to the integral over the mean absorbed dose.

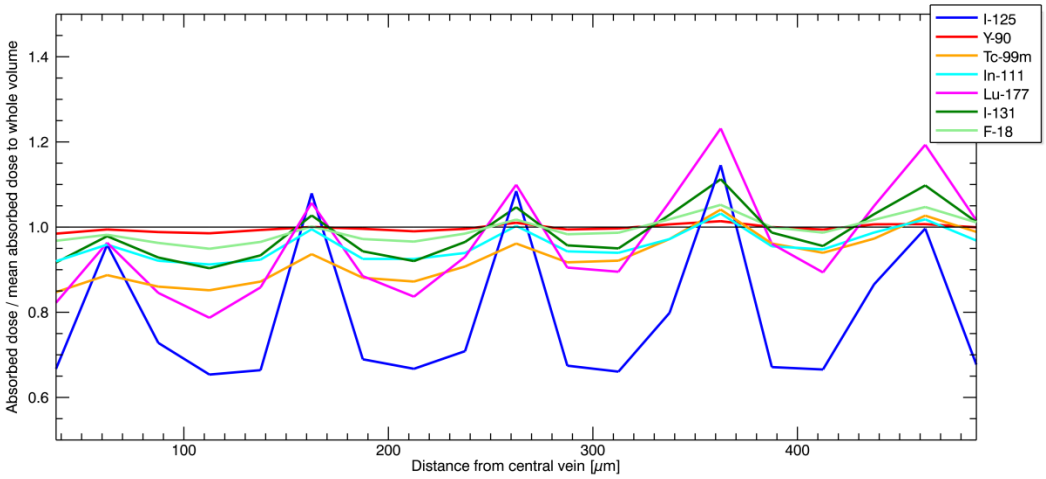

Figure 4.21. A graphical illustration of the ratio of the locally absorbed dose in the hepatocytes divided by the mean absorbed dose to the whole volume from activity distributed on the five Kupffer cell positions [n0:n4].

The absorbed dose ratio in the hepatocytes is radionuclide and position specific. For ^{125}I the absorbed dose ratio will the lowest between at the positions between the Kupffer cells, a pattern seen also for the other nuclides included. The main structure in the model is the hepatocytes and therefore the absorbed dose to this structure for many of the nuclides will be quite close to the mean dose of the total volume.

Due to the design of the model, a slight wedge shape could be seen in the graph, with an increasing absorbed dose ratio around the Kupffer cell placed at 355 μm from CV. Taking a closer look at the flux distribution for the different nuclides, an increase can be seen close to the wedge corner, where, due to the positioning of Kupffer cells a slightly higher concentration of active cells can be seen. Since the cell number in the four quadrants in the circle in figure 4.22 is the same, the absorbed dose ratio within those cells will be slightly higher than for cells at another radial distance from the central vein. This effect can also be seen for $^{99}Tc^{m}$ in figure 4.15.

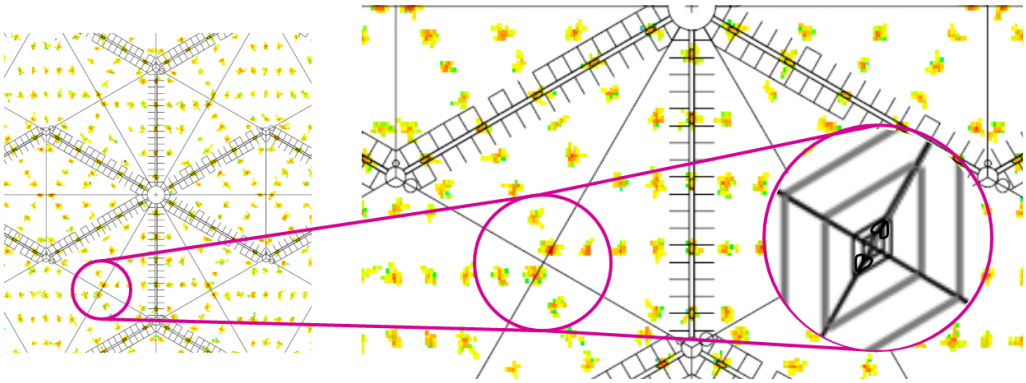

Figure 4.22. A graphical illustration of the flux distribution (particles/cm^2 for the electron component of ^{125}I) close to a wedge corner, where parts of four Kupffer cells are positioned. This will give rise to a locally higher flux, which in turn will result in a slightly higher absorbed dose in the hepatocytes close to the corner, which due to the numbering of cells will have the same number.

The dose ratio for Space of Disse is presented in figure 4.23. It will be the highest for ^{125}I, followed by ^{177}Lu and ^{111}In. The dose ratio for the Kupffer cell closest to the portal fields, n4, is lower due to its position centered at the border of two hepatocytes.

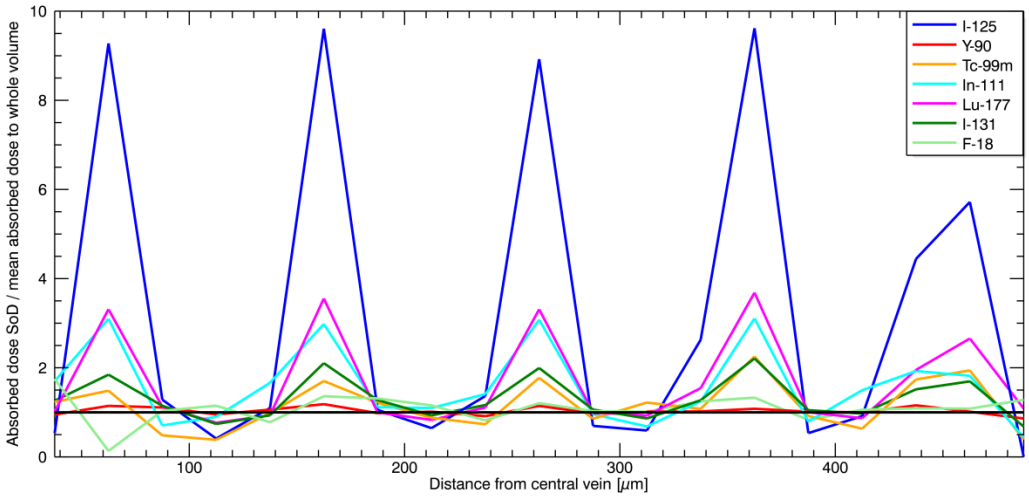

Figure 4.23. A graphical illustration of the ratio of the locally absorbed dose in the Space of Disse divided by the mean absorbed dose to the whole volume from activity distributed on the five Kupffer cell positions [n0:n4].

The absorbed self-dose to the Kupffer cell can also be simulated and is of interest for the possible comparison to other absorbed dose calculations of the Kupffer cells performed by others, *e.g.* Gardin *et al.* [6] and Makrigiorgos *et al.*. A diagram of the self-dose ratio between the locally absorbed dose and the mean absorbed dose to the whole liver volume for all five Kupffer cell positions can be seen in figure 4.24.

The selfdose ratio will be as highest for ^{125}I, but interesting is the quite high ratios received for the diagnostically used nuclides; ^{99}Tc^{m} and ^{111}In. Especially interesting is the comparison between these two nuclides and nuclides today used for therapies; *e.g.* ^{177}Lu and ^{131}I. The biological implication of this is still unknown, and thus no further conclusion will be drawn concerning these simulation results.

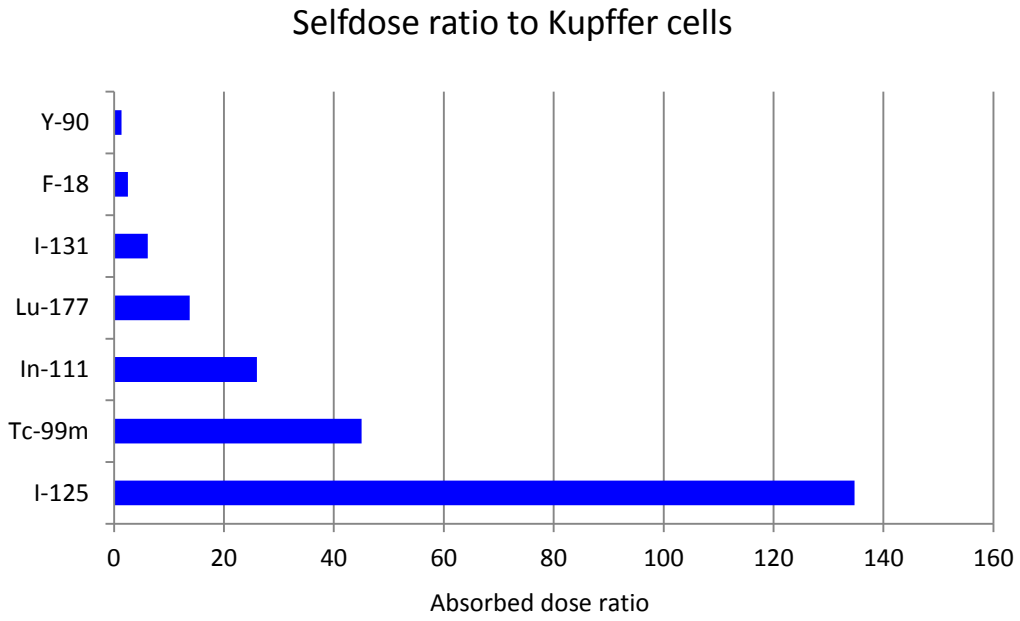

Figure 4.24. The diagram shows the self-dose ratio between the locally absorbed dose and the mean absorbed dose to the whole liver volume for the Kupffer cells. The different radionuclides are found on the y-axis, plotted against the value of the dose ratio.

Since the endothelial cells around the central vein is thought to be the main target for the development of RILD, the absorbed dose ratio for the CV for different activity distributions is of great interest. Two cases can be seen below, in figure 4.25 with activity inside the Kupffer cells and in figure 4.26 with activity in the portal artery, simulating the microsphere treatment situation.

For ^{90}Y the absorbed dose ratio for CV is very close to the mean absorbed dose, whereas for ^{177}Lu there will be a big difference between the mean absorbed dose and the dose absorbed in the CV.

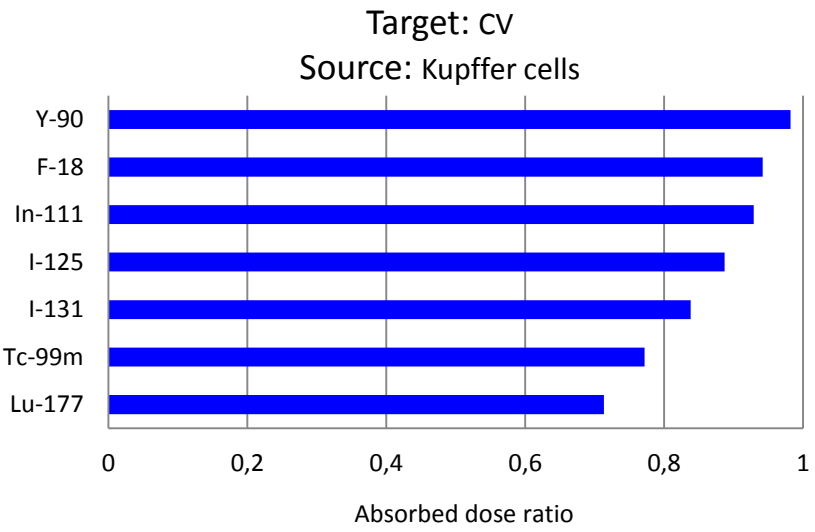

Figure 4.25. The diagram shows the absorbed dose ratio between the locally absorbed dose in the CV and the mean absorbed dose to the whole volume. The activity is accumulated in the five different Kupffer cell positions [n0:n4].

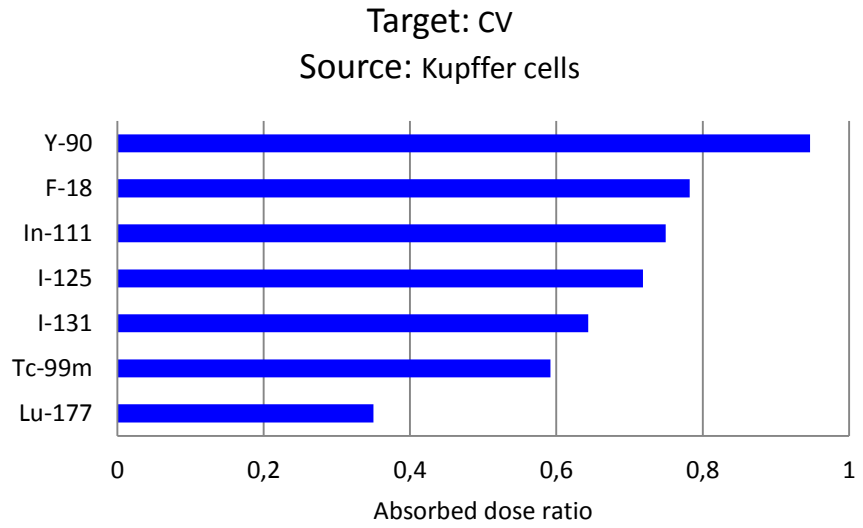

Figure 4.26. The diagram shows the absorbed dose ratio between the locally absorbed dose in the CV and the mean absorbed dose to the whole volume. The activity is accumulated in the portal artery framing the hepatic lobule.

To estimate the dependence of lobule position; central versus peripheral inside the liver volume, the absorbed dose distribution from a sphere with homogeneous, tissue equivalent composition has been simulated. The phantom, with a radius of 20 cm is consisting of 500 μm thick shells and is having an inner delimitation, with the radius equal to the radius of the liver volume (6 cm) containing a homogeneous distribution of the different radionuclides. The radial distribution of the absorbed dose, normalized to an average absorbed dose of 1 Gy, for the different components of the decay is plotted in figure 4.27.

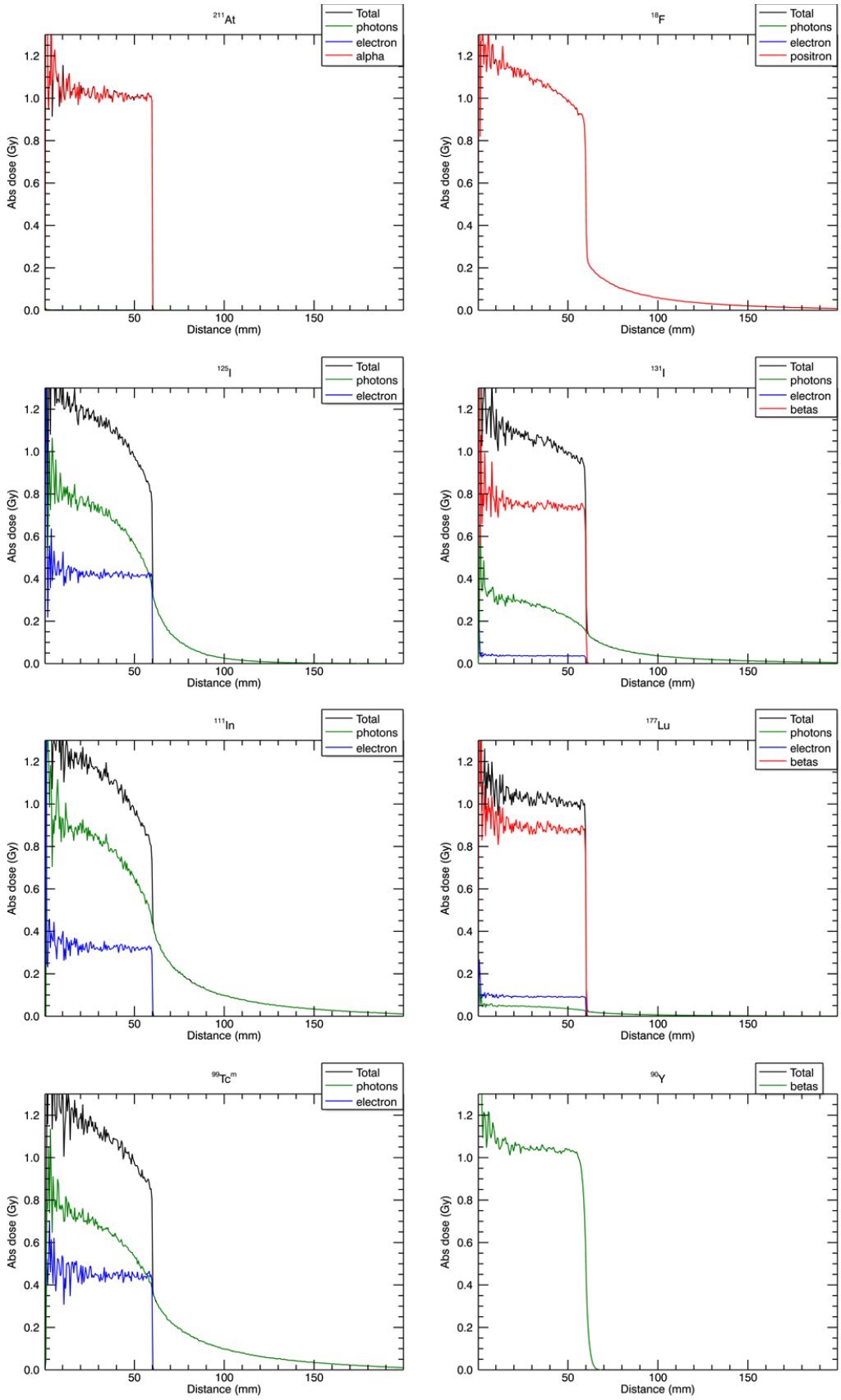

Figure 4.27. Each sub-picture is showing the radial distribution of the absorbed dose originating from a sphere (radius 6 cm) with homogeneous activity distribution. The black line shows the total absorbed dose, and the colored different part of the decay. The colors are not consistent throughout the figure; therefore see each sub-label.

For the nuclides ^{211}At, ^{177}Lu and ^{90}Y the absorbed dose rapidly decreases outside the active sphere, indicating a little loss of absorbed energy for the lobules at the periphery. For ^{125}I, ^{131}I, ^{111}In and ^{99}Tc^{m} the photon component of the decay just outside the simulated liver volume will deliver a dose of approximately 15-45% of the mean absorbed dose. For the other decay components, the absorbed dose will be distributed within the liver volume. For ^{18}F, just outside the liver volume, the absorbed dose will be approximately 20 % of the mean absorbed dose, decreasing to zero within 20 cm. The quite ragged appearance of the curves is due to bad statistics within the smallest shells close to the origin.

Since the source during the simulations, due to the dose reciprocity theorem, is placed only in the most central seven lobules, the spill out of absorbed dose from the photon component is assumed to be even less than presented above.

The dosimetric calculations found in the literature concerning the absorbed self-dose to Kupffer cells active in the ^{99}Tc^{m} labeled radiopharmaceutical uptake [5, 6] differs a lot, although both studies are indicating a large difference between the conventional dosimetry calculations for the average dose in the whole organ, compared to the dose calculation on a cellular level. Gardin *et al.* [6] proposed an absorbed dose ratio of about 15000 whereas the calculations performed by Makrigiorgos *et al.* [5] indicated that conventional dosimetry calculations underestimate the absorbed dose to the Kupffer cells 8- to 30-fold.

The result achieved in this study is to be found within the quite large interval, since the absorbed dose ratio in the Kupffer cells for ^{99}Tc^{m} is 45.

5 Conclusions

Monte Carlo simulations concerning locally absorbed dose, mainly the ratio of the local absorbed dose divided by the absorbed dose to the whole liver volume was carried out with the small-scale dosimetry model created. The model is suitable for absorbed dose calculations where the activity distribution in a volume is inhomogeneous and the many different structures can act as source.

The model is quite flexible and many source-target combinations can be defined, thus allowing both cross-dose and self-dose calculations. The dimensions of the defined structures are easily changed, making the model non-rigid and not solely depending on the dimensions found during the literature search performed in the start-up moment of this project. The flexibility of the model also allows for the addition of pathological areas within the lobule, for a possible expansion of the absorbed dose calculations

The absorbed dose calculations performed shows a divergence between the locally absorbed dose calculated with the created small-scale dosimetry model and the conventional absorbed dose calculation presenting the mean absorbed dose. This tendency of the result received with the small-scale dosimetry model is in line with the results obtained with other small-scale dosimetry models created, [10-13], all concluding that absorbed dose calculations based on small-scale dosimetry models differs from the conventional dosimetric methodologies calculating an average absorbed dose for a larger structure.

The absorbed dose ratios received in this study, there the Kupffer cells, the space of Disse, the hepatocytes and the central vein is used as target and the Kupffer cells and the portal artery is used as source, shows a noteworthy inhomogeneous absorbed dose distribution. The mean absorbed dose to the whole volume is seen to both over- and under estimate the local absorbed dose. Examples are a 135-fold underestimation of the self-absorbed dose to Kupffer cells containing ^{125}I, where at the same time the hepatocytes placed between the Kupffer cells is receiving an absorbed dose of about 0.7 times the mean dose. The absorbed dose ratio is deeply radionuclide dependent, as well as depending on source-target-combination, indicating that each case will need an individualized analysis.

6 Discussion

Important to keep in mind when observing the design, as well as the simulation results of the created small-scale dosimetry model, is that the model is a simplification of sketches drawn of the liver parenchyma, sketches that can be found in various textbooks, which in turn is a simplification of the, quite structured, still chaotic inseparable continuum building the structure of the liver tissue. But with support from literature concerning distribution, accumulation and cell structures acting as targets, this small-scale dosimetry model still provides a realistic approach for a more detailed dosimetry, still using the MIRD formalism, which could bring some understanding of the heterogeneous absorbed dose distribution originating from the heterogeneous activity distribution.

The model is based on the concept of the hepatic lobule and the division of one lobule, made in this project, to only six wedges seemed good enough for the application of this study, even though all infinitesimal points in the periphery of the lobule really ought to be on an axis between the central vein and the portal field. The dosimetric approach was not considered to be affected of that angular simplification done, and especially not since the model already is simplified compared to the reality.

The cellular distribution and the morphological volume density achieved in the created small-scale dosimetry model is considered to be satisfactory for the purpose of this study, since the main differences occurs due to the not included blood and bile vessel networks inside the liver. The model created was based on the idea of the hepatic lobule, since the main region of interest for this study concerning the locally absorbed dose distribution is the different part of this lobule, consisting of the different cell types discussed in the theory chapter. Also noteworthy is that not all cell types present in the hepatic lobule was included in the created model, another factor of importance for the diverging volume densities between biological lobules and the model lobule. Only cells considered to be of importance either for becoming source of for being target was included and the selection was based on the literature search, the baseline of this study.

The dimensions of structures included in the model many times are the mean value of values originating from collected data from different sources and therefore should not be taken to be perfectly accurate. The sinusoids and the bile canaliculi are microstructures with a gradient in diameter size along the lobule axis from central vein to portal tract. In the model on the other hand, these structures are having the same diameter throughout the whole lobule. The dosimetric consequence of the selection of mean value is needed to be examined, *i.e.* the uncertainty of the achieved result should be investigated based on the selected dimensions. Since the model created is moldable, the dimensions of different microstructures easily could be changed from the smallest to the largest possible dimension and the question of the dosimetric implication of dimension could be answered.

Concerning the number of Kupffer cells and their distribution in the hepatic lobule, a discussion is justified. The distribution in the lobule is dependent on the nutrient and oxygen gradient present in each lobule, due to the direction of blood flow. In the periportal region, where the concentrations of oxygen and nutrients are at its highest, also the concentration of Kupffer cells is at its highest. Around the center of each lobule, where the oxygen and nutrient concentrations is at its lowest, also the concentration of Kupffer cells is at its lowest, *i.e.* the concentration of Kupffer cells depends on the acinus zones. The percentage distribution within these zones, published by Dancygier [21], was said to be: 43% in the periportal zone 1, 32% in zone 2 and 25% in perivenous zone 3. The borders of these three zones however are not outlined, making the reproduction of the distribution hard to implement. The small-scale dosimetry model created does not fulfill this

distribution to the letter, but decreasing concentration of Kupffer cells with increasing distance from the portal field is achieved.

The volume density of the Kupffer cells in the model is quite low compared to the volume density found in the literature, but taking into account the fraction of Kupffer cells assumed to be active in the radiopharmaceutical uptake. According to Makrigiorgos [5] the fraction of the liver occupied by radiolabeled Kupffer cells were found to be between 0,001 and 0,01 and found by Gardin *et al.* [6] to be 0,2%, values corresponding to the included volume density of Kupffer cells included in the model, and since the density [g/cm^3] of the Kupffer cells in the model is equal to the density of the hepatocytes and the space of Disse, with only a slight difference from the density [g/cm^3] of the blood, the non-active Kupffer cells was decided not to be included.

The results received, when simulating activity accumulated in the Kupffer cells is depending on the on the radial distribution of the active cells. In this model all the Kupffer cells, since based on a repeated geometry, is placed at the same radial distance from the central vein and are therefore stacked up each other. A fact definitely affecting the results received.

The lymphatic system of the liver is not included in the model, since the origin of the lymph is suggested to be in the space of Disse, a structure already included in the model. After the creation the transport of the lymph through the lobule is not associated with any dedicated canals, until it reaches the lymphatic vessels in the portal tract. According to this information the lymphatic system could be simulated by already existing cells.

The accuracy of the simulations carried out by the created small-scale dosimetry model needs to be confirmed to some golden standard, which by exemplary manners is a biological method enabling analyze of the biological effect close to areas with a high accumulated uptake. The amount of cell damage close to the partially stationary hot spots in the liver tissue, created by the Kupffer cells, is of great interest for the reasoned relevance of the model. Hence, the actual question is; dose the higher absorbed dose to a region in the liver tissue show an increased level of damage?

The relevance of the high self-dose to the Kupffer cells accumulating radionuclides is also so far questionable. Questions needed to be answered are questions like; what happens to a Kupffer cell after accumulation of high activities and what happens to the radiopharmaceutical when what happen to the Kupffer cell happens. The life time of Kupffer cells is said to averages several months [21], while one, at the same time consider the uptake of ^{232}Th rich contrast agent, accumulated in the Kupffer cells to deliver lifelong exposure to the exposed human [43]. The mechanism behind this is of great interest and of great value for the understanding of the activity distribution and re-distribution within the tissue.

In radionuclide therapies many variables are involved in the final expression of the biological effect occurring from targeted radionuclides accumulated in the tissue or targeted radionuclides passing by on its way to the target region. Important to keep in mind is the possibility that the most important variables when trying to determine the biological effect are biological rather than dosimetric; therefore making dosimetry not the only parameter responsible for response [44]. When analyzing the results from a dosimetric calculation carried out with a new dosimetry model, *e.g.* a small-scale dosimetry model, it is of great importance to be aware of the duality concerning the origin of the biological effect. Since, on a model basis, it is possible to calculate the absorbed dose on a microstructural scale, it will be of great relevance to be able to understand and distinguish between the responses dominated by biological factors versus response that can be traced down to dosimetric factors, all in all, to be able to predict the effect resulting from the absorbed dose.

Having a cellular or subcellular perspective, this small-scale dosimetry model is way to macroscopic for the interpretation of biological effects originating from irradiation. Instead a dosimetric model modeling the different cellular compartments would be required and as long as the source and target regions not are becoming too small, so that the statistical fluctuation of the decay and the energy deposition increases, it would be a possibility. Even more important then, than now, would be to find the accurate source and target regions, for the absorbed dose calculation to be as accurate as possible and for the results to be as interpretable as possible.

An important question thus needed to be answered is how important the quantity absorbed dose *per se* is and more specific if it is an appropriate quantity to use for the predicting of biological response. Maybe one should put more interest in other quantities, or a combination of quantities, such as radiosensitivity of different tissues, the radiation quality and dose rate in combination with the subcellular distribution.

A process of possible importance for the biological effect is the apoptosis, a controlled mechanism eliminating single cells of the tissue without any inflammatory response. The apoptotic process must, due to its efficiency, be highly controlled for the mechanism not to be augmented nor suppressed, since any change from the controlled apoptosis could both contribute to the induction and exaggeration of an acute or chronic disease [45].

Transformation and proliferation can be promoted if the mechanism of apoptosis is inhibited, a proliferation characterizing hepatocellular carcinoma (HCC). Significantly in primary HCCs was a mutation leading to loss of the tumor suppressor gene p53, making the rate of apoptosis decrease, thereof could a modulation of the apoptosis signaling molecules be an input of new the treatments of HCCs [45]. Irradiation can in some cells induce apoptosis, but it is highly cell-dependent and is commonly seen to be p53-dependent [46], whereas a positive effect for HCCs having a loss of p53 can be discussed, as well as the side effects to healthy tissue. The roll of apoptosis in a dose-response relationship therefore needs to be investigated before the absorbed dose can be used as a measurement for the biological effect.

Also kept in mind when discussing mechanisms responsible for the biological effect, should be both the bystander effect and the theory of hormesis. Concerning the bystander effect, where non-irradiated cells adjacent to irradiated cells may express cell damage and eventually move in to apoptosis. The bystander effect is expressed by intracellular communication, such as direct transfer of small molecules or ions by gap junction communication and extracellular communication by excretion of signaling factors, such as hormones and growth regulators [47]. The biological implications of the bystander effect and its relation to the absorbed dose still needs to be investigated before it can be included in any dose-response model.

Also important for the interpretation of the biological effect due to exposure of genotoxic agents (direct action by covalently binding to DNA) or non-genotoxic agents (indirect nature of action, not involving the DNA attack) is the theory of hormesis; the beneficial effect of low dose exposure to toxins. Several *in vivo* studies have shown supporting results for the inhibition of hepatocarcinogenesis after a low dose exposure of a non-genotoxic carcinogen, possible explained by adaptive response. A non-genotoxic agent is associated with a perfect threshold and exposure to doses below the threshold would not induce any damage. Irradiation increasing the concentration of reactive oxygen species (ROS), in principle a genotoxic substance, may increase the general repair capacity of the tissue and evolving repair systems for oxidative base modification and chromosome breaks, irrespective of damage. The induction of low doses of ROS in a rat liver have also been

seen to decrease the cell proliferation [47]. The biological effect expressed after irradiation therefore are not only depending on the absorbed dose, thus a lot of other mechanisms are involved in the final response expressed.

Even though the results obtained by the MC simulation still not are validated against any biological data, the results still are indicating a large difference between the mean absorbed dose to the whole volume compared to the locally absorbed dose, a difference of potential clinical value. Dosimetry models useful for meaningful predictability concerning absorbed dose to both the normal and pathological tissue within an organ will be a necessity for future treatment planning; for optimization of treatment results as well as for absorbed dose minimization to organs at risk.

In order for the dosimetry to become more involved in the treatment planning of therapies, the understanding of the dose-response relationship needs to be improved, including understanding of how factors such as dose rate, linear energy transfer, particle range, biodistribution and radiosensitivity of both normal cells and tumor cells affects the dose-response. Also the scale of dosimetry needed for dose-response understanding; *e.g.* organ, microstructure, cellular or subcellular, needs to be investigated.

A good relationship between physicians and physicists will be required for these questions to be answered, particularly given that the answers with almost certainly will be treatment as well as population dependent, implying an individual dose-response characterization. But all in all, the creation of the small-scale dosimetry model is one step closer to the future of a more sophisticated dosimetry in nuclear medicine and radiation protection.

7 Outlook

The small-scale dosimetry model of the liver tissue created in the project is just one of the first steps taken on the way towards a better understanding of the radiobiological effects occurring after irradiation of liver tissue. The outlook of this project therefore extends to both the near future as well as it diverges into a complex mesh of possible projects for the overall future. The extensions for the near future are applications of the small-scale dosimetry model created, whereas the extensions for the overall future regard the confirmation of simulation results against a golden standard, an investigation which also would imply an indication of what scale of dosimetry will be needed for dose-response understanding.

Simulated S-values (Gy MBq^{-1}) will in the near future be presented for different source-target combinations for some common radionuclides important in radionuclide therapy and diagnostics. The S-value describes the mean absorbed dose per unit cumulated activity in the source region, thus acting as dose-conversion factors and can straightforwardly be presented in table form.

The dosimetric implication of the dimensions chosen for the microstructures defined in the model needs to be investigated and hence the uncertainty in the results achieved. The absorbed fraction and thus the absorbed dose in the different microstructures are closely connected to the dimensions of the structures involved, whereas a small change in dimension could imply a great change in the absorbed fraction. The accuracy of the simulation results then deeply is connected to the dimensions chosen.

A theoretical study, possible and interesting, would concern the radionuclide ^{232}Th, a naturally abundant isotope decaying through the emission of an alpha-particle, and a component in the contrast agent Thorotrast (thorium (^{232}Th) dioxide colloid; rectangular crystals measuring approximately 2 μm along maximum dimension) used in diagnostic x-ray during the 1920s to the 1940s [22]. After injection, the Thorotrast aggregates were incorporated mainly within the mononuclear phagocyte system in the liver, including the Kupffer cells, and in the spleen and lymph nodes [43]. The physical half-life of ^{232}Th is $1{,}4 \cdot 10^{10}$ years [42], whereupon a deposition results in a lifelong and continuous low dose rate alpha particle irradiation [43], a statement interesting since the life time of the Kupffer cells is appreciated to be some months [21]. Studies of patient exposed to Thorotrast have shown an increased risk developing liver cancer, particularly cholangiocarcinoma, but also angiosarcoma and hepatocellular carcinoma [43], indicating that the Thorotrast is one of the most carcinogenic agents ever delivered to humans [22]. The dosimetry is considered complex because of the strongly heterogenic distribution of radiopharmaceuticals, therefore considered a perfect application for the small-scale dosimetry model created.

For the overall future the expansion of the project will be in the direction of investigating the biological effect of the heterogeneous radiopharmaceutical and hence the heterogeneous absorbed dose distribution. Ionizing radiation will induce various forms of DNA damage in the exposed tissue; among others DNA single strand breaks and double strand breaks (DSB), and it is suggested that DSBs are the dominating damage leading to cell death. The DSBs are possible to detect and measure, *e.g.* by the use of the DNA repair histone H2AX, which in the vicinity of a DSB rapidly will be phosphorylated to γH2AX, therefore acting as a marker for the DSBs [48]. Expectantly, this would be a method suitable for the measurement of the biological effect due to the absorbed dose in the liver tissue, thus one should be aware of the binucleate nature of the hepatocytes. If one, at the same time could detect the distribution of the radiopharmaceutical, either by

autoradiography or by fluorescence, one could possible deduce if there is an increased level of DNA damage in areas close to hot spots in the liver tissue.

Noteworthy for future analyzes of the liver lobule in combination with irradiation is the, in the lobule existing oxygen gradient, due to the direction of blood flow. Nutrient and oxygen rich blood is entering the lobule in the portal tracts and leaving trough the central vein in its center. The concentration of oxygen therefore is at its highest in the periphery of the lobule, decreasing towards the center, see figure 2.3.

Known as the oxygen effect is the correlation of the level of oxygen within a tissue and the radiosensitivity of the cells. A lower presence of oxygen will decrease the radiosensitivity, implying that a more hypoxic condition, in contrast to an aerated condition, will need higher absorbed doses to achieve the same biological effect. The ratio of absorbed doses needed for the same biological effect in differently oxygenated tissues, hypoxic/aerated, is called the oxygen enhancement ratio [46].

The oxygen rich structures in the periphery of the lobule, the part of the lobule most rich in Kupffer cells is accumulating the largest part of the radiopharmaceutical, and are therefore exposed to more radiation than the cells closer to the central vein. Interesting would be, if the level of damage in the periportal areas; oxygenated, and therefore more sensitive to radiation and at the same time exposed to more irradiation due to the inflow of blood and a higher concentration of Kupffer cells, would show an increased level of damage maybe explainable by the oxygen effect.

The outlook of this project, extending both to the near future and to the overall future contains a lot of interesting questions, questions which seems possible to answer and in turn probably will induce even more interesting questions.

Acknowledgements

I would like to express my gratitude and appreciation to my supervisors Bo-Anders Jönsson, Erik Larsson and Sven-Erik Strand, for their invaluable knowledge and experience in the field of this project and for their never-ending source of new approaches and ideas concerning the model making and its usage.

A special thanks to my supervisor Erik Larsson for his patience and good knowledge of programming in general and of the simulations method used in particular. Also his knowledge concerning removal of Trojan horses was of good help and appreciation during this semester.

I would also like to take the opportunity to thank M.D Pehr Rissler at Skånes University Hospital in Lund, who in the start-up process of this project contributed with fruitful discussions concerning the morphology and pathology of the hepatic tissue.

Also I would like to thank Johan Knutsson, the love and treasure of my life, for patiently having followed me through the ups and downs of this master thesis project, which eventually, in a photomontage edition, ended up on his desktop.

To my parents at the countryside of Småland, I would like to send thanks regarding the never-ending help and support received though the years; whether concerning studies and the definition of luck or the input of common sense in situations where that was not so common.

I would also, last but definitely not least, like to thank my roomies in the basement, with whom I have shared office with this semester and hence spent a lot of long, but rather interesting hours with. Without you this project had been carried out in more quiet peace and depression.

Bibliography

1. Bolch, W.E., et al., *MIRD pamphlet No. 21: a generalized schema for radiopharmaceutical dosimetry--standardization of nomenclature.* J Nucl Med, 2009. **50**(3): p. 477-84.
2. Loeevinger, R. and Berman, M., *A schema for absorbed-dose calculations for biologically-distributed radionuclides.* J Nucl Med, 1968: p. Suppl 1:9-14.
3. Jönsson, B.A., Strand, S.E. and Larsson, B.S., *A quantitative autoradiographic study of the heterogeneous activity distribution of different indium-111-labeled radiopharmaceuticals in rat tissues.* J Nucl Med, 1992. **33**(10): p. 1825-33.
4. Hindie, E., et al., *Microautoradiographic study of technetium-99m colloid uptake by the rat liver.* J Nucl Med, 1988. **29**(6): p. 1118-21.
5. Makrigiorgos, G.M., et al., *Inhomogeneous deposition of radiopharmaceuticals at the cellular level: experimental evidence and dosimetric implications.* J Nucl Med, 1990. **31**(8): p. 1358-63.
6. Gardin, I., et al., *Dosimetry at the cellular level of Kupffer cells after technetium-99m-sulphur colloid injection.* J Nucl Med, 1992. **33**(3): p. 380-4.
7. Howell, R.W., Rao, D.V. and Sastry, K.S., *Macroscopic dosimetry for radioimmunotherapy: nonuniform activity distributions in solid tumors.* Med Phys, 1989. **16**(1): p. 66-74.
8. Wisse, E., *Kupffer cell reactions in rat liver under various conditions as observed in the electron microscope.* J Ultrastruct Res, 1974. **46**(3): p. 499-520.
9. Burt, A.D., Portmann, B.C. and Ferrell, L.D., *MacSween's Pathology of the Liver*. 6th ed: Churchill Livingstone, Elsivier, 2012.
10. Jönsson, L., et al., *A dosimetry model for the small intestine incorporating intestinal wall activity and cross-doses.* J Nucl Med, 2002. **43**(12): p. 1657-64.
11. Larsson, E., et al., *A small-scale anatomic model for testicular radiation dosimetry for radionuclides localized in the human testes.* J Nucl Med, 2012. **53**(1): p. 72-81.
12. Larsson, E., et al., *Dosimetry calculations on a tissue level by using the MCNP4c2 Monte Carlo code.* Cancer Biother Radiopharm, 2005. **20**(1): p. 85-91.
13. Stubbs, J.B., Evans, J.F. and Stabin, M.G., *Radiation absorbed doses to the walls of hollow organs.* J Nucl Med, 1998. **39**(11): p. 1989-95.
14. Gulec, S.A., et al., *Hepatic structural dosimetry in (90)Y microsphere treatment: a Monte Carlo modeling approach based on lobular microanatomy.* J Nucl Med, 2010. **51**(2): p. 301-10.
15. Howell, R.W., *The MIRD Schema: from organ to cellular dimensions.* J Nucl Med, 1994. **35**(3): p. 531-3.
16. Murthy, R., et al., *Yttrium-90 microsphere therapy for hepatic malignancy: devices, indications, technical considerations, and potential complications.* Radiographics, 2005. **25 Suppl 1**: p. S41-55.
17. Emami, B., et al., *Tolerance of normal tissue to therapeutic irradiation.* Int J Radiat Oncol Biol Phys, 1991. **21**(1): p. 109-22.
18. International Commission on Radiation Units and Measurements, *ICRU Report No 67. Absorbed-dose Specification in Nuclear Medicine*2002: Nuclear Technology Pub.
19. Mescher, A.L., *Junqueira's Basic Pathology. Text & Atlas*. 12th ed 2010: The McGraw-Hill Companies.
20. Kiernan, F., *The Anatomy and Physiology of the Liver.* Philosophical Transactions of the Royal Society of London, 1833. **123**(ArticleType: research-article / Full publication date: 1833 /): p. 711-770.
21. Dancygier, H., *Microscopic Anatomy*, in *Clinical Hepatology* 2010, Springer Berlin Heidelberg. p. 15-51.

22. Fajardo L. F., Berthrong M. and Anderson R.E., *Radiation Pathology. 2001*: Oxford University Press, Inc.
23. Braet, F. and Wisse, E., *Structural and functional aspects of liver sinusoidal endothelial cell fenestrae: a review.* Comp Hepatol, 2002. **1**(1): p. 1.
24. Rappaport, A.M., et al., *Subdivision of hexagonal liver lobules into a structural and functional unit; role in hepatic physiology and pathology.* Anat Rec, 1954. **119**(1): p. 11-33.
25. Schiff, E.R., Maddrey, W.C. and Sorrell, M.F., *Schiff's Diseases of the Liver*. 11th ed: Wiley-Blackwell. p. 109.
26. *Basic anatomical and physiological data for use in radiological protection: reference values. A report of age- and gender-related differences in the anatomical and physiological characteristics of reference individuals. ICRP Publication 89.* Ann ICRP, 2002. **32**(3-4): p. 5-265.
27. Menzel, H.G., Clement, C. and DeLuca, P., *ICRP Publication 110. Realistic reference phantoms: an ICRP/ICRU joint effort. A report of adult reference computational phantoms.* Ann ICRP, 2009. **39**(2): p. 1-164.
28. Ludwig, J., et al., *Anatomy of the human biliary system studied by quantitative computer-aided three-dimensional imaging techniques.* Hepatology, 1998. **27**(4): p. 893-9.
29. Reed, G.B. and Cox A. J., *The human liver after radiation injury. A form of veno-occlusive disease.* Am J Pathol, 1966. **48**(4): p. 597-611.
30. Kennedy, A.S., et al., *Pathologic response and microdosimetry of (90)Y microspheres in man: review of four explanted whole livers.* Int J Radiat Oncol Biol Phys, 2004. **60**(5): p. 1552-63.
31. Welsh, J.S., Kennedy A. S. and Thomadsen B., *Selective Internal Radiation Therapy (SIRT) for liver metastases secondary to colorectal adenocarcinoma.* Int J Radiat Oncol Biol Phys, 2006. **66**(2 Suppl): p. S62-73.
32. ICRU, *Fundamental Quantities and Units for Ionizing Radiation*, Report 85. Volume 11. No 1. 2011.
33. Snyder, W.S., et al., *"S" Absorbed Dose Per Unit Cumulated Activity for Selected Radionuclides and Organs.* MIRD Pamphlet No.11. Society of Nuclear Medicine, 1975.
34. Larsson, E., *Realistic tissue dosimetry models using Monte Carlo simulations - applications for radionuclide therapies*, in *Department of Medical Radiation, Physics Clinical Sciences, Lund.* PhD Thesis. 2011, Lund University, Sweden.
35. Roeske, J.C., et al., *Small-scale dosimetry: challenges and future directions.* Semin Nucl Med, 2008. **38**(5): p. 367-83.
36. X-5 Monte Carlo Team, *MCNP - A General Monte Carlo N-Particle Transport Code,.* Version 5, Volume I: Overview and therory, Los Alamos National Laboratory report, LA-UR-03-1987.
37. Pelowitz, D.B., *MCNPX User's Manual.* 2008: p. Version 2.6.0, Los Alamos National Laboratory report, LA-CP-07-1473.
38. Brown, F.B., *Fundamentals of Monte Carlo Particle Transport,.* Lecture Notes for Monte Carlo course, Los Alamos National Laboratory report, LA-UR-05-4983: p. Available at URL: http://mcnp-green.lanl.gov/publication/pdf/LA-UR-05-4983_Monte_Carlo_Lectures.pdf (2005).
39. X-5 Monte Carlo Team, *MCNP - A General Monte Carlo N-Particle Transport Code,.* Version 5, Volume II: User's Guide, Los Alamos National Laboratory report, LA-CP-03-0245.
40. M.J Berger et al. *Stopping-Power and Range Tables for Electrons, Protons and Helium Ions*. October 7, 2009; Available from: http://www.nist.gov/pml/data/star/index.cfm.

41. Chu, S.Y.F., Ekström, L.P. and Firestone, R.B. *The Lund/LBNL Nuclear Data Search*. 1999; Version 2.0:[Available from: http://nucleardata.nuclear.lu.se/toi/.
42. Firestone, R.B., *Table of Isotopes CD-ROM* Eighth Edition: 1999 Update: Wiley-Interscience.
43. UNSCEAR 2006 REPORT Vol. 1., *Effects of ionizing radiation: Annex A - Epidemiological studies of radiation and cancer.* UNSCEAR; 2006.
44. Sgouros, G., *Dosimetry of internal emitters.* J Nucl Med, 2005. **46 Suppl 1**: p. 18S-27S.
45. Schattenberg, J.M., Galle, P.R. and Schuchmann, M., *Apoptosis in liver disease.* Liver Int, 2006. **26**(8): p. 904-11.
46. Hall, E., *Radiobiology for the Radiologist.* 2006, Sixth Edition: Lippincott Williams & Wilkins a Wolter Kluwer business.
47. Fukushima, S., et al., *Hormesis and dose-response-mediated mechanisms in carcinogenesis: evidence for a threshold in carcinogenicity of non-genotoxic carcinogens.* Carcinogenesis, 2005. **26**(11): p. 1835-45.
48. Sak, A. and Stuschke, M., *Use of gammaH2AX and other biomarkers of double-strand breaks during radiotherapy.* Semin Radiat Oncol, 2010. **20**(4): p. 223-31.